České vysoké učení technické v Praze
Fakulta jaderná a fyzikálně inženýrská
Katedra matematiky

Mathematical Modelling of Mobility of Martensitic Microstructures

Diplomová práce

Ondřej Glatz

Vedoucí práce:	Ing. Hanuš Seiner, Ph.D. (ÚT AV ČR, KMAT FJFI)
Konzultant:	Ing. Michal Landa, CSc. (ÚT AV ČR)
Akademický rok:	2009/2010

Prohlašuji, že jsem předloženou práci vypracoval samostatně a že jsem uvedl veškerou použitou literaturu.

V Praze dne 5. 1. 2010

Ondřej Glatz

I would like to thank my supervisor Ing. Hanuš Seiner, PhD., and my consultant Ing. Michal Landa, CSc. for their willingness, patience, and support.

Contents

List of Symbols

Symbol	Description
a, b, c, α, β, γ	scalar values
$\mathbf{u}$, $\mathbf{v}$	vector values
$\mathbf{A}$, $\mathbf{B}$	matrices
$\mathbb{R}$, $\mathbb{Z}$, $\mathbb{N}$	set of real, integral, and natural numbers
$\mathbf{u}\cdot\mathbf{v}$, $\mathbf{u}\times\mathbf{v}$	standard dot product and cross product of vectors $\mathbf{u}$ and $\mathbf{v}$
$\mathbf{u}\otimes\mathbf{v}$	dyadic product of vectors $\mathbf{u}$ and $\mathbf{v}$
$\mathbf{I}$	identity matrix in $\mathbb{R}^3$ (identity)
u_k, a_{ij}, A_{ij}	vector components and matrix elements
(a_{ij}), (A_{ij})	matrix with elements a_{ij} and A_{ij}
$\det\mathbf{A}$, $\operatorname{rank}\mathbf{A}$, $\operatorname{tr}\mathbf{A}$	determinant, rank, and trace of matrix $\mathbf{A}$
$\ker\mathbf{A}$	kernel of matrix $\mathbf{A}$
$\mathbf{A}^{-1}$, $\mathbf{A}^{\mathrm{T}}$	inverse and transpose of matrix $\mathbf{A}$
$\mathbf{A}^{-\mathrm{T}}$, $\operatorname{adj}\mathbf{A}$	inverse transpose and adjoint matrix
$\partial\Omega$, Ω^{C}	boundary and complement of set Ω
Ω°, $\overline{\Omega}$	interior and closure of set Ω
$\frac{\partial\mathbf{y}_j}{\partial x_i}$, $\partial_{x_i}\mathbf{y}_j$	derivative of $\mathbf{y}_j$ with respect of $\mathbf{x}_i$
$\nabla\mathbf{y}$	gradient of function $\mathbf{y}$ (see definition 1.1.1)
$\mathcal{L}(\mathbf{e}_1,\mathbf{e}_2,\mathbf{e}_3)$	crystal lattice generated by vectors $\mathbf{e}_1$, $\mathbf{e}_2$, and $\mathbf{e}_3$
$G(\mathbf{e}_i)$, $L(\mathbf{e}_i)$	space group and Laue group of lattice $\mathcal{L}(\mathbf{e}_1,\mathbf{e}_2,\mathbf{e}_3)$
L_A, L_M	point group of austenite and martensite
$\{\mathbf{A}{:}\mathbf{B}\}$	twinning system comprising gradients $\mathbf{A}$ and $\mathbf{B}$
ε_{ij}, ϵ_{ij}	Cauchy's small strain tensor, Lagrangian finite strain tensor
C_{ijkl}	stiffness tensor

Introduction

In this thesis we investigate particular types of so called martensitic microstructures observed during the experiments on copper-aluminium-nickel shape memory alloy single crystal. The reversible martensitic phase transition and related martensitic microstructure stand behind the all of interesting properties of the shape memory alloys—the unique class of smart materials, which is a subject of intensive research in the last years. We believe that the better understanding of the microstructure formation and evolution contributes towards the further expansion of the shape memory alloys applications in industry as well as in a common life.

Our aim is to provide tools to treat microstructures which violate premises of the widely adopted model of microstructures in equilibrium state developed by Ball and James [4]. This model is intended to assess admissibility of given microstructure type and to predict its parameters. However, there were experimentally observed microstructures, which are not admissible according to this classical model. To solve this issue we propose a slight modification, which enable us to handle also these *incompatible* microstructures.

Besides the equilibrium microstructure model, also the dynamical model of the microstructure evolution is constructed. Since we need to describe spontaneous evolution of the microstructure without external loads applied, as occurring in experiments [19], we have to develop the model at a faster time scale ([16]) than most of others. This leads us to incorporate the rate-dependent dissipation mechanism into the model.

Chapter 1

Introduction to Martensitic Phase Transition

This chapter summarises the mathematical description of the reversible martensitic transition theory developed particularly by Ball and James [4]. It extends some parts of author's bachelor thesis [9].

1.1 Continuum Mechanics

Most of the theoretical framework used in this thesis is formulated in the terms of continuum mechanics. Thus it is necessary to introduce some basics used in the context of the martensitic transition.

1.1.1 Deformation, Deformation Gradient

The essential terms we are using are the *deformation* and the *deformation gradient.*

Definition 1.1.1. A homeomorphism $\mathbf{y}\colon\ \mathbf{x} \to \mathbf{y}(\mathbf{x})$ on $\Omega \subset \mathbb{R}^n$ into $\mathbb{R}^n$ is called deformation, if $y_{i|\mathcal{G}_k^\circ} \in C^{(2)}(\mathcal{G}_k^\circ)$, where $\mathcal{G}_k^\circ$ are open connected sets (regions) in $\mathbb{R}^n$ and $\bigcup_{k=1}^r \mathcal{G}_k = \Omega$, $r \in \mathbb{N}$. Further we require that $\det \mathbf{F}(\mathbf{x}) > 0 \quad \forall\ \mathbf{x} \in \mathcal{G}_k^\circ$. The matrix $\mathbf{F}(\mathbf{x}) = \nabla \mathbf{y}(\mathbf{x})$ is defined as

$$\mathbf{F}(\mathbf{x}) = \nabla \mathbf{y}(\mathbf{x}) = \begin{pmatrix} \frac{\partial y_1}{\partial x_1} & \frac{\partial y_1}{\partial x_2} & \cdots & \frac{\partial y_1}{\partial x_n} \\ \frac{\partial y_2}{\partial x_1} & \frac{\partial y_2}{\partial x_2} & \cdots & \frac{\partial y_2}{\partial x_n} \\ \vdots & \vdots & \ddots & \vdots \\ \frac{\partial y_n}{\partial x_1} & \frac{\partial y_n}{\partial x_2} & \cdots & \frac{\partial y_n}{\partial x_n} \end{pmatrix} \qquad \text{for short: } F_{ij} = \frac{\partial y_i}{\partial x_j}\,. \tag{1.1}$$

The matrix $\mathbf{F}(\mathbf{x})$ is called the deformation gradient.

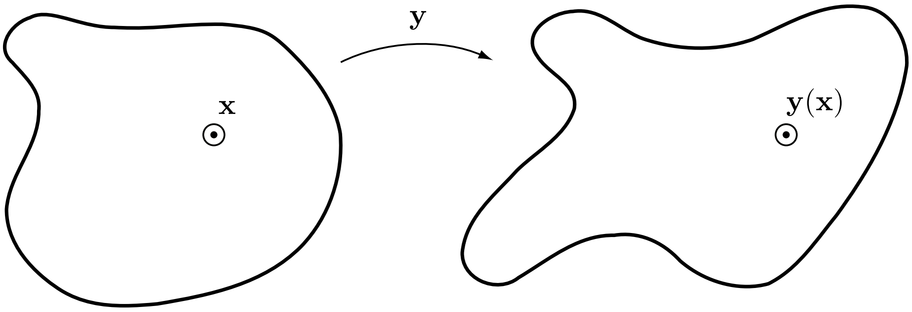

Figure 1.1: Deformation of a body [6]

Let Ω be a subset of $\mathbb{R}^n$ representing a body before the deformation. Then, if $\mathbf{x} \in \Omega$ is a point of the body in reference configuration, the $\mathbf{y}(\mathbf{x})$ is the corresponding point of the deformed body (see Fig. 1.1). Instead of the deformation $\mathbf{y}$ the *displacement field*

$$\mathbf{u}(\mathbf{x}) = \mathbf{y}(\mathbf{x}) - \mathbf{x} \tag{1.2}$$

is often used.

1.1.2 Local Properties of Deformation

If deformation gradient $\mathbf{F}(\mathbf{x})$ is continuous in a point $\mathbf{x}$, it characterises the deformation on the infinitesimal neighbourhood of this point, and

$$\mathrm{d}\mathbf{y} = \mathbf{F}(\mathbf{x})\,\mathrm{d}\mathbf{x} \tag{1.3}$$

holds.

Since the value of $\det \mathbf{F}(\mathbf{x})$ is equal to the Jacobian of the deformation, it describes a volume change of the neighbourhood of the point $\mathbf{x}$. We can write

$$\mathrm{d}\widetilde{V} = (\det \mathbf{F})\,\mathrm{d}V\ , \tag{1.4}$$

where $\mathrm{d}\widetilde{V}$ stands for an infinitesimal volume of the deformed body, and $\mathrm{d}V$ denotes the respective volume in the reference configuration (for clarity the arguments are omitted, but keep in mind that in general all used quantities are functions of position in the reference configuration).

Thereafter, the text is restricted to deformations in $\mathbb{R}^3$. For the volume of an infinitesimal parallelepiped

$$\mathrm{d}\widetilde{V} = (\mathrm{d}\mathbf{y}_1 \times \mathrm{d}\mathbf{y}_2)\cdot\mathrm{d}\mathbf{y}_3 \tag{1.5}$$

(here, vectors $\mathrm{d}\mathbf{y}_i$ correspond to edges of given volume) we can derive formula (1.4) using (1.3).

An infinitesimal parallelogram of area $\mathrm{d}\widetilde{S}$, with normal $\widetilde{\mathbf{n}}$ can be written as

$$\mathrm{d}\widetilde{\mathbf{S}} = \widetilde{\mathbf{n}}\,\mathrm{d}\widetilde{S} = \mathrm{d}\mathbf{y}_1 \times \mathrm{d}\mathbf{y}_2\,. \tag{1.6}$$

Analogously to (1.4), we obtain the formula for transformation of surface elements by deformation $\mathbf{y}$:

$$\mathrm{d}\widetilde{\mathbf{S}} = (\det \mathbf{F})\mathbf{F}^{-\mathrm{T}}\mathrm{d}\mathbf{S}\,. \tag{1.7}$$

The deformation is called *homogeneous*, if the deformation gradient is independent on $\mathbf{x}$ (i.e. $\mathbf{F}(\mathbf{x})$ is constant on body Ω). Then, the mapping $\mathbf{y}$ is an affine transformation:

$$\mathbf{y}(\mathbf{x}) = \mathbf{F}\mathbf{x} + \mathbf{x_0} \qquad \mathbf{F} \in \mathbb{R}^{n,n},\ \mathbf{x_0} \in \mathbb{R}^n\,. \tag{1.8}$$

Let the point $\mathbf{x}$ be a point of continuity of the deformation gradient. Then, we can consider the deformation to be homogeneous on the infinitesimal neighbourhood of $\mathbf{x}$. As mentioned above, such deformation is an affine transform of the neighbourhood of the point $\mathbf{x}$. Every affine transform can be decomposed into pure stretch, a following rotation, and a final translation by vector $\mathbf{x_0}$ from (1.8). This unique decomposition is obtained by application of theorem 1.1.1 to the deformation gradient $\mathbf{F}$.

Theorem 1.1.1 (Polar decomposition)**.** *Let* $\mathbf{F}$ *be a regular, real matrix;* $\det \mathbf{F} > 0$. *Then, there exists a unique symmetric positive definite matrix* $\mathbf{U}$ *and an orthogonal matrix* $\mathbf{R}$*,* $\det \mathbf{R} = 1$ *(i.e.* $\mathbf{R}$ *is a proper rotation), such that*

$$\mathbf{F} = \mathbf{R}\mathbf{U}\,, \tag{1.9}$$

where $\mathbf{U} = \sqrt{\mathbf{F}^{\mathrm{T}}\mathbf{F}}$ *and* $\mathbf{R} = \mathbf{F}\mathbf{U}^{-1}$.

The matrix $\mathbf{U}$, often called the *Bain matrix (tensor)*, represents just metric properties of the deformation on the neighbourhood of $\mathbf{x}$. Rotation $\mathbf{R}$ and vector $\mathbf{x_0}$ (in (1.8)) carry the information on the transformation of the neighbourhood as a whole.

1.1.3 Kinematic Compatibility of Gradients

Consider a deformation $\mathbf{y}$ defined on region Ω which is homogeneous on regions $\mathcal{G} \subset \Omega$ and $\mathcal{G}^{\mathrm{C}} = \Omega \backslash \overline{\mathcal{G}}$, where $\partial\mathcal{G}$ is a part of a sufficiently smooth hypersurface. Let us examine the relation between the gradients $\mathbf{F}$ and $\mathbf{G}$ corresponding to the deformations $\mathbf{y}_{|\mathcal{G}}$ and $\mathbf{y}_{|\mathcal{G}^{\mathrm{C}}}$ respectively.

Since the deformation is continuous, the surface $\partial\mathcal{G}$ has to transform equally "from both sides" (see Fig. 1.2). Let $\mathbf{z} \in \partial\mathcal{G}$, $\mathbf{n}$ be a normal to $\partial\mathcal{G}$ in the point $\mathbf{z}$. If $\mathcal{T}$ is a tangent plane to $\partial\mathcal{G}$ at the point $\mathbf{z}$ (hence $\mathbf{n}$ is a normal of $\mathcal{T}$), for all vectors $\mathbf{t}$ from

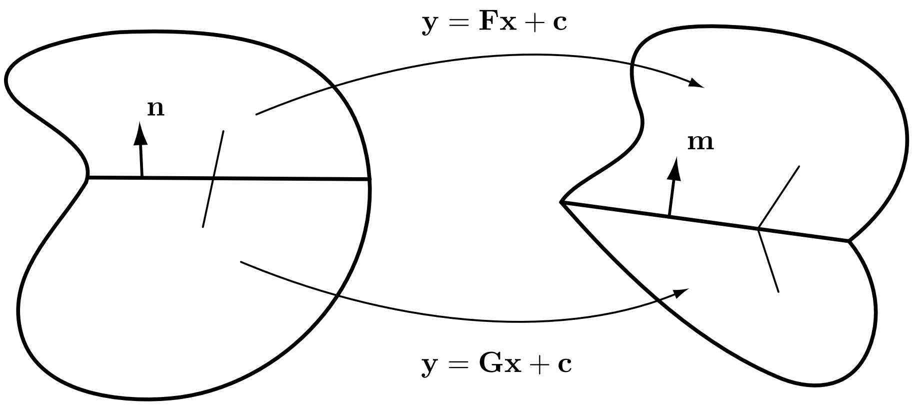

Figure 1.2: Compatibility of gradients [6]

the tangent space of $\mathcal{T}$ the relation $\mathbf{Ft} = \mathbf{Gt}$ has to hold. This can be expressed by the *Hadamard jump condition*

$$\exists\, \mathbf{a} \in \mathbb{R}^3 : \ \mathbf{F} - \mathbf{G} = \mathbf{a} \otimes \mathbf{n}\,, \tag{1.10}$$

where $\otimes$ denotes *dyadic product* defined below.

Definition 1.1.2. Binary operation $\otimes : \ \mathbb{R}^n \times \mathbb{R}^n \to \mathbb{R}^{n,n}$ defined by formula

$$\mathbf{u} \otimes \mathbf{v} = \mathbf{u}\mathbf{v}^{\mathrm{T}} = \begin{pmatrix} u_1v_1 & u_1v_2 & \dots & u_1v_n \\ u_2v_1 & u_2v_2 & \dots & u_2v_n \\ \vdots & \vdots & \ddots & \vdots \\ u_nv_1 & u_nv_2 & \dots & u_nv_n \end{pmatrix} \qquad \forall\, \mathbf{u}, \mathbf{v} \in \mathbb{R}^n\,, \tag{1.11}$$

is called the dyadic product of vectors $\mathbf{u}$ and $\mathbf{v}$.

One can see that

$$\operatorname{rank}(\mathbf{a} \otimes \mathbf{b}) \leq 1\,. \tag{1.12}$$

Therefore, we can write the Hadamard condition equivalently as

$$\operatorname{rank}(\mathbf{F} - \mathbf{G}) \leq 1\,. \tag{1.13}$$

According to the findings above, $\ker(\mathbf{F} - \mathbf{G})$ is a tangent space of $\partial\mathcal{G}$ at every point in $\partial\mathcal{G}$ (supposing $\mathbf{F} \neq \mathbf{G}$). Since $\mathbf{F}$ and $\mathbf{G}$ are constant, the tangent space remain same at all points in $\partial\mathcal{G}$. Hence $\partial\mathcal{G}$ has to be a part of plane.

If constant matrices $\mathbf{F}$ and $\mathbf{G}$ are prescribed, a deformation $\mathbf{y}$ homogeneous on some regions $\mathcal{G}, \mathcal{G}^{\mathrm{C}} \in \Omega$ with gradients $\mathbf{F}$ and $\mathbf{G}$ exists if and only if the Hadamard condition (1.13) or (1.10) is fulfilled for some vectors $\mathbf{a}, \mathbf{n} \in \mathbb{R}^3$. Then, the surface, which separates $\mathcal{G}$ and $\mathcal{G}^{\mathrm{C}}$, is a plane with normal $\mathbf{n}$ (after the deformation, the normal changes, using (1.7), to $(\det \mathbf{F})\mathbf{F}^{-\mathrm{T}}\mathbf{n}$). Gradients $\mathbf{F}$ and $\mathbf{G}$ satisfying the Hadamard condition are called *compatible.*

We need to extend the idea of compatibility to symmetric positive definite matrices $\mathbf{U}_a$ and $\mathbf{U}_b$, which come from the polar decomposition (see 1.1.1) of the corresponding deformation gradients. The question is, if there exist rotations $\mathbf{R}_1$ and $\mathbf{R}_2$ such that matrices $\mathbf{F} = \mathbf{R}_1\mathbf{U}_a$ and $\mathbf{G} = \mathbf{R}_2\mathbf{U}_b$ are compatible gradients. When

$$\mathbf{R}_1\mathbf{U}_a - \mathbf{R}_2\mathbf{U}_b = \mathbf{a} \otimes \mathbf{n} \tag{1.14}$$

holds for some rotations, we call the matrices $\mathbf{U}_a$ and $\mathbf{U}_b$ compatible.

This redefinition of the compatibility for symmetric positive definite matrices is more general. Thus, there is no simple criterion (like the Hadamard jump condition) for this new compatibility. Some more complex criteria are mentioned in section 1.3.3.

1.2 Continuum Mechanics and Crystal Structure

Since this work deals with monocrystalline material, we need to introduce basic properties of crystalline solids into our description in the terms of the continuum mechanics. Especially, the effects of a crystal lattice symmetries are important.

1.2.1 Crystal Lattice

For simplicity, in this section we are considering an *ideal crystal*, which is of infinite size and has a periodic structure without defects. The characteristic property of such ideal crystal is a repetition of some basic *motif* in the directions of crystallographic axes. The motif can be asymmetric comprising number of atoms.

Consider three linearly independent vectors $(\mathbf{e}_1, \mathbf{e}_2, \mathbf{e}_3)$ defining the elementary translations in the crystallographic axes directions. Then the set

$$\mathcal{L}(\mathbf{e}_1, \mathbf{e}_2, \mathbf{e}_3) = \{\mu_1\mathbf{e}_1 + \mu_2\mathbf{e}_2 + \mu_3\mathbf{e}_3 \mid \mu_i \in \mathbb{Z}\}\,. \tag{1.15}$$

form a three-dimensional grid. By placing a selected motif at the all grid points the ideal crystal is obtained. This grid is called the *crystal lattice.* Equivalently: *The crystal lattice is a set of points, which have identical and identically oriented neighbourhood.* The generating vectors are called *lattice vectors* or *primitive basis.*

The lattice direction is understood as a direction defined by two distinct lattice points. Likewise, *the lattice plane* is understood as a plane defined by three affine independent lattice points.

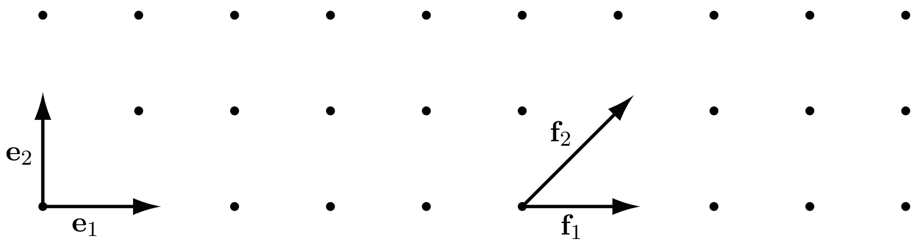

Figure 1.3: Crystal lattice and lattice vectors [6]

1.2.2 Crystal Symmetries

It is apparent that two different triplets of vectors can generate identical lattices. See example in Fig. 1.3 (in 2D), where the same lattice is generated by vectors $(\mathbf{e}_1, \mathbf{e}_2)$ as well as by vectors $(\mathbf{f}_1, \mathbf{f}_2)$. Let us explore the relation between such triplets. The following definition comes in useful for this.

Definition 1.2.1 (primitive unit cell)**.** The primitive unit cell of a crystal lattice is a parallelopiped defined by respective lattice vectors.

Let $(\mathbf{e}_1, \mathbf{e}_2, \mathbf{e}_3)$ and $(\mathbf{f}_1, \mathbf{f}_2, \mathbf{f}_3)$ be triplets such that

$$\mathcal{L}(\mathbf{e}_1, \mathbf{e}_2, \mathbf{e}_3) = \mathcal{L}(\mathbf{f}_1, \mathbf{f}_2, \mathbf{f}_3) \,. \tag{1.16}$$

Then each vector in the first triplet must be a integral linear combination of vectors from the second triplet:

$$\mathbf{e}_i = \mu_{ij}\mathbf{f}_j \qquad \mu_{ij} \in \mathbb{Z} \,. \tag{1.17}$$

This ensures that the set $\mathcal{L}(\mathbf{e}_1, \mathbf{e}_2, \mathbf{e}_3)$ is a subset of $\mathcal{L}(\mathbf{f}_1, \mathbf{f}_2, \mathbf{f}_3)$. To achieve an equality in (1.16) one more condition has to be added. The necessary and sufficient condition for the equality (1.16) is (1.17) along with the condition

$$|\det(\mu_{ij})| = 1 \,, \tag{1.18}$$

where (μ_{ij}) denotes a matrix in $\mathbb{Z}^{3,3}$ with coefficients μ_{ij}. This tells us that primitive unit cells of both lattices have the same volume. It is easy to see that the matrices (μ_{ij}) form a multiplicative group. This group is denoted S.

Another useful groups are the symmetry groups of the lattice. First, we must define what is understood by the *lattice symmetry.*

Definition 1.2.2 (lattice symmetry)**.** Lattice symmetry is an affine map on $\mathbb{R}^3$ into $\mathbb{R}^3$, which maps the lattice back to itself.

For example, the elementary translations by lattice vectors are possible symmetries for all lattices. It is essential to distinguish between the lattice symmetries and symmetries of atoms spatial arrangement. Because of a possible asymmetry of the motif, the atoms spatial arrangement adopts, in general, only the translational lattice symmetries.

From the text above, it follows that a regular linear map $\mathbf{H}$ is a symmetry of lattice $\mathcal{L}(\mathbf{e}_1, \mathbf{e}_2, \mathbf{e}_3)$ if and only if

$$\exists\,(\mu_{ij}) \in S : \mathbf{H}\mathbf{e}_i = \mu_{ij}\mathbf{e}_j\,. \tag{1.19}$$

The set of all lattice symmetries as well as the set of all regular linear maps forms a group. Thus, we can define the group of all *linear lattice symmetries* (or the group of matrices representing these symmetries):

$$G(\mathbf{e}_i) = G(\mathbf{e}_1, \mathbf{e}_2, \mathbf{e}_3) = \{\mathbf{H} \in \mathbb{R}^{3,3} \mid \exists\,(\mu_{ij}) \in S : \mathbf{H}\mathbf{e}_i = \mu_{ij}\mathbf{e}_j\}\,. \tag{1.20}$$

A more important group than the *space group* $G(\mathbf{e}_i)$ is its finite subgroup containing only proper rotations:

$$L(\mathbf{e}_i) = L(\mathbf{e}_1, \mathbf{e}_2, \mathbf{e}_3) = \{\mathbf{Q} \in G(\mathbf{e}_i) \mid \mathbf{Q} \in SO(3)\}\,. \tag{1.21}$$

This group is called the *Laue group* of crystal lattice. One can show that there exist only 11 distinct Laue groups. These are further divided into 7 known crystal systems (for further details see [22]).

Since there is a possibility that no primitive unit cell has the same symmetries as a whole lattice, it is convenient to define a *conventional unit cell.* The conventional unit cell respects lattice symmetries and it is the smallest such cell. Type of the conventional cell determines the lattice crystal system. Volume of the conventional cell is a multiple of the primitive cell volume.

1.2.3 Cauchy–Born Hypothesis

Here we introduce a theorem that links continuum mechanics to crystallography and vice versa. It is called the *Cauchy–Born hypothesis*, see [6] for another formulation.

Theorem 1.2.1 (Cauchy–Born)**.** *Let a crystal occupy region a* $\Omega \subset \mathbb{R}^3$ *in the reference configuration, and let* $\mathbf{y}$ *be a deformation on* Ω*. For all* $\mathbf{x} \in \Omega$ *consider crystal lattice in the neighbourhood of* $\mathbf{x}$*. The lattice is generated by vectors* $\mathbf{e}_1^0(\mathbf{x})$, $\mathbf{e}_2^0(\mathbf{x})$, $\mathbf{e}_3^0(\mathbf{x})$*. Let* $\mathbf{e}_1(\mathbf{x})$, $\mathbf{e}_2(\mathbf{x})$, $\mathbf{e}_3(\mathbf{x})$ *denote corresponding vectors generating a lattice of the deformed crystal in the neighbourhood of* $\mathbf{y}(\mathbf{x})$*. Then, for these vectors the following formula holds:*

$$\mathbf{e}_i(\mathbf{x}) = \mathbf{F}(\mathbf{x})\,\mathbf{e}_i^0(\mathbf{x})\,, \tag{1.22}$$

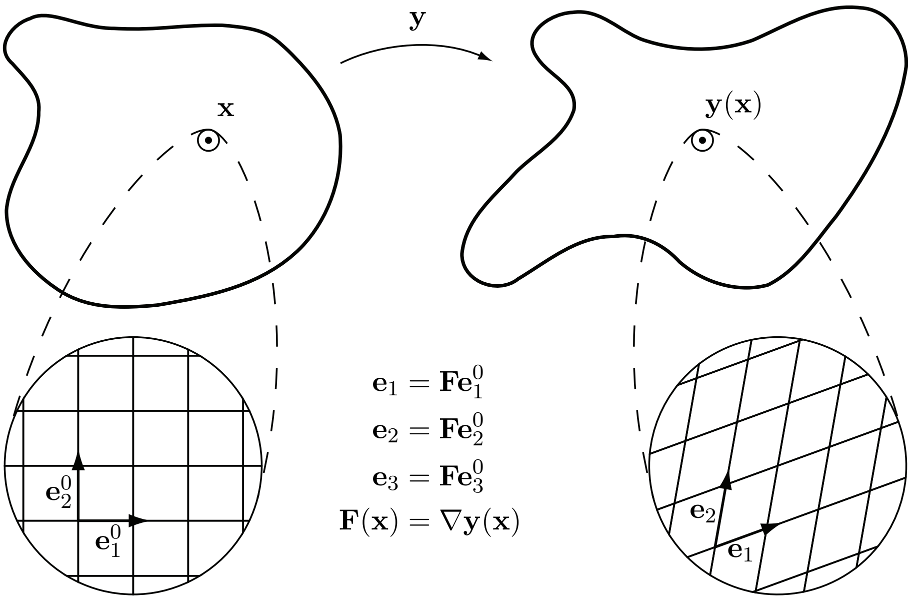

Figure 1.4: Cauchy–Born hypothesis [23]

where $\mathbf{F}(\mathbf{x}) = \nabla\mathbf{y}(\mathbf{x})$ *is a gradient of the deformation at the point* $\mathbf{x}$*. Conversely, if two triplets of vectors generating distinct lattices are given, then equation* (1.22) *defines deformation* $\mathbf{y}(\mathbf{x}) = \mathbf{F}\mathbf{x}$*, which maps the first lattice to the second one.*

See Fig. 1.4 for a schematic outline of the idea. It means that the primitive unit cell of the deformed lattice is an image of the original unit cell under the linear mapping $\mathbf{F}(\mathbf{x})$.

1.3 Reversible Martensitic Transition

The martensitic transition is a first-order, solid to solid phase transition. During this transition, the latent heat is released and the lattice parameters and first derivatives of thermodynamic potentials change discontinuously.

The main property of the martensitic transition is that it is *diffusionless.* There are no long distance transfers of atoms; the character of the chemical bonds in the crystal does not change. In the case of the reversible transition, no defects occur in lattice. Also, almost no volume change takes place during the transition. Hence, the reverse transformation can proceed in a similar manner. During the martensitic phase transition the lattice parameters are slightly changed. According to the Cauchy–Born hypothesis 1.2.1, this leads to well defined macroscopic deformation. Parameters of the deformation are determined from the material parameters.

The transition process can be invoked by a temperature change or by mechanical loading. This work focuses on thermally induced transitions. The high temperature phase is called *austenite* and the low temperature phase is called *martensite*. Regarding the transitions under investigation, the Laue group of martensite has to be a proper subgroup of the Laue group of austenite (see [7]).

1.3.1 Mathematical Description of Transition

We can represent the reversible martensitic phase transition as a crystal body deformation in the sense of definition 1.1.1. The transition properties mentioned above enable us to do this. The sets $\mathcal{G}_k^\circ$ from definition 1.1.1 correspond to the regions in material, which are transformed to regions with uniform lattice. On these regions the deformation is homogeneous.

As a reference configuration we choose the crystal in the austenite phase. An arbitrary state of the crystal after the phase transition can be then interpreted as a deformation $\mathbf{y}$ of the original state.

Let $(\mathbf{e}_1^0, \mathbf{e}_2^0, \mathbf{e}_3^0)$ be vectors generating crystal the lattice in region $\mathcal{G}_k^\circ$ of the reference configuration and let $(\mathbf{e}_1, \mathbf{e}_2, \mathbf{e}_3)$ be respective lattice vectors in the corresponding region of the transformed crystal. According to the Cauchy–Born hypothesis (see 1.2.1), mapping $\mathbf{F}$ defined by relation

$$\mathbf{e}_i = \mathbf{F}_k \mathbf{e}_i^0 \tag{1.23}$$

is the gradient of deformation $\mathbf{y}$ on region $\mathcal{G}_k^\circ$.

Gradients $\mathbf{F}_k$ define deformation on individual regions $\mathcal{G}_k^\circ$ up to translations, which are determined from the requirement of continuity of resulting deformation.

Within the scope of continuum mechanics the phase transition of region Ω is fully described by a finite set of compatible gradients and corresponding regions. Admissible configurations are limited by material constants and by the compatibility conditions from section 1.1.3.

Regarding the condition on martensite symmetries noted at beginning of this section, possible deformation gradients are restricted to a sufficiently small neighbourhood of identity such that the Laue group of deformed lattice is a proper subgroup of the Laue group of original lattice. Such neighbourhood is called the *Ericksen–Pitteri neighbourhood*. An rigorous definition can be found in [6].

Deformation gradients on regions, which stay in austenite, have a form of pure rotation (lattice can be rotated, but the lattice parameters do not change). Gradients belonging to martensite regions have a nontrivial polar decomposition (see 1.1.1). Thus, the positive definite part $\mathbf{U}$ is different from identity the matrix. If two gradients have

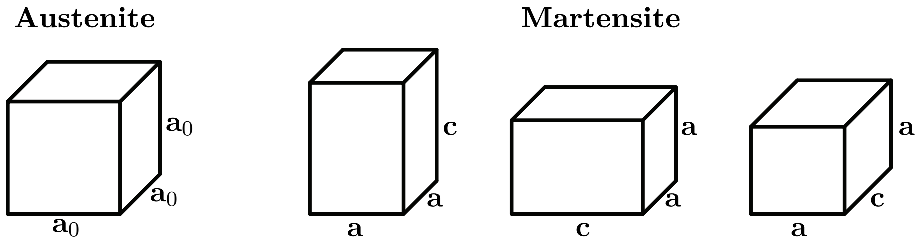

Figure 1.5: Variants of martensite (cubic austenite, tetragonal martensite) [6]

the same positive definite parts, the corresponding lattices are mutually rotated lattices of identical parameters; converse does not hold. We call the lattices, which are up to rotation identical, *equivalent.*

1.3.2 Variants of Martensite

Thanks to the higher symmetry of austenite we can obtain (by distinct, small deformations from the Ericksen–Pitteri neighbourhood) a set of distinct but equivalent lattices, which are "far" from each other. This means that the rotations mapping these lattices one to another are large—far from identity. These lattices correspond to different *variants of martensite.* See example in Fig. 1.5, where the transformation from cubic to tetragonal crystal system is illustrated. From the cubic austenite, three distinct variants of martensite are obtained.

Thus we identify the individual variants with Bain matrices **U** from the polar decomposition 1.1.1 of respective deformation gradients.

Let matrix **U** be one of the variants of martensite. It holds (see [10]) that the set $\mathcal{M}$ of all possible variants can be constructed as

$$\mathcal{M} = \{\mathbf{Q}^{\mathrm{T}}\mathbf{U}\mathbf{Q} \mid \mathbf{Q} \in L_A\}\,, \tag{1.24}$$

where L_A is the Laue group of austenite. Hence, every two variants of martensite are similar with similarity transformation from L_A. The number of elements in $\mathcal{M}$, i.e. the number n of possible martensite variants is equal to a quotient of group orders L_A and L_M:

$$n = \frac{|L_A|}{|L_M|}\,, \tag{1.25}$$

where L_M denotes the Laue group of martensite.

1.3.3 Twins, Twinning Systems

If deformation gradients corresponding to distinct variants of martensite are compatible, various regions of the material can transform to these different variants. See the

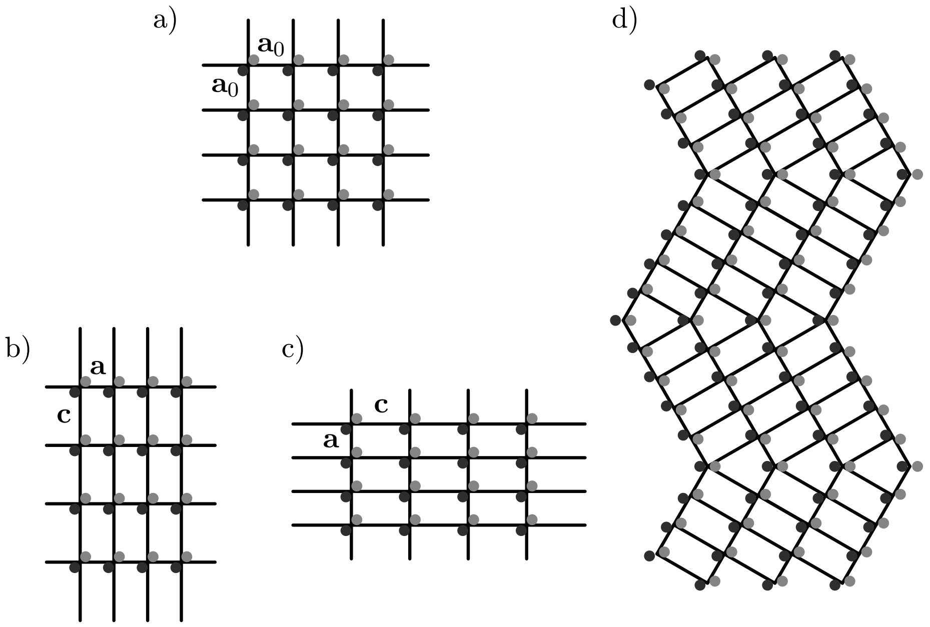

Figure 1.6: Twinning system (a—austenite; b, c—variants of martensite; d—resulting deformation) [6]

example of such deformation in Fig. 1.6. Recall that the interfaces between homogeneously deformed regions are necessarily planar (see 1.1.3).

In the section 1.1.3 a more general compatibility condition for positive definite matrices was formulated in the following form:

$$\exists\, \mathbf{R}_1, \mathbf{R}_2 \in \mathbb{R}^{3,3}, \mathbf{a}, \mathbf{n} \in \mathbb{R}^3 : \; \mathbf{R}_1\mathbf{U}_a - \mathbf{R}_2\mathbf{U}_b = \mathbf{a} \otimes \mathbf{n}\,. \tag{1.26}$$

This is exactly the condition, which tells us, if two given variants of martensite can create the system of martensite–martensite interfaces from Fig. 1.6 (d).

Such variants we call *twins*, the respective system of transformed regions is called a *twinning system*. The main twinning systems usually distinguished in literature are:

Type I twins The interface is a lattice plane.

Type II twins Vector **a** is a lattice direction.

Compound twins Vector **a** is a lattice direction and the interface is a lattice plane.

In the case of the cubic to monoclinic transition the fourth possible type can appear, where neither vector **a** is a lattice direction nor the interface is a lattice plane, but such a case is rather rare. The types differ in range of mechanical properties.

Let $\mathbf{U}_a$ and $\mathbf{U}_b$ be Bain matrices representing two different variants of martensite. According to the definition, two rotations—$\mathbf{R}_1$, $\mathbf{R}_2$—and two vectors—$\mathbf{n}$, $\mathbf{a}$—such that Hadamard condition (1.26) holds must be found to decide on compatibility of the variants. Or reversely, a nonexistence of these elements must be proved.

Multiplying the equation (1.26) by matrix $\mathbf{R}_2^{\mathrm{T}}$ from the left we get

$$\widetilde{\mathbf{R}}\mathbf{U}_a - \mathbf{U}_b = \widetilde{\mathbf{a}} \otimes \mathbf{n}\,, \tag{1.27}$$

where

$$\widetilde{\mathbf{R}} = \mathbf{R}_2^{\mathrm{T}}\mathbf{R}_1\,, \tag{1.28a}$$

$$\widetilde{\mathbf{a}} = \mathbf{R}_2^{\mathrm{T}}\mathbf{a}\,. \tag{1.28b}$$

Vector $\mathbf{n}$ does not change. The solution of the new equation (1.27) represents a whole class of solutions of the original equation (1.26); one of the rotations in (1.26) can be chosen arbitrarily, and then the second one and the vector $\mathbf{a}$ are determined from (1.28).

The following theorem ([6]) gives an exhaustive answer to our question of solvability of (1.27), but it is quite complicated.

Theorem 1.3.1 (Ball, James)**.** *Let $\mathbf{U}_a$ and $\mathbf{U}_b$ be positive definite matrices. Denote*

$$\mathbf{C} = \mathbf{U}_b^{-1}\mathbf{U}_a^2\,\mathbf{U}_b^{-1}\,, \tag{1.29}$$

let $\lambda_1 \leq \lambda_2 \leq \lambda_3$ be the eigenvalues of $\mathbf{C}$.

Then $\mathbf{U}_a$ and $\mathbf{U}_b$ are compatible if and only if $\mathbf{C} \neq \mathbf{I}$ and $\lambda_2 = 1$. Further, if $\mathbf{U}_a$ and $\mathbf{U}_b$ are compatible, the equation (1.27) has exactly two solutions $(\widetilde{\mathbf{R}}_1, \widetilde{\mathbf{a}}_1, \mathbf{n}_1)$ and $(\widetilde{\mathbf{R}}_2, \widetilde{\mathbf{a}}_2, \mathbf{n}_2)$. Where

$$\widetilde{\mathbf{a}}_i = \rho\left(\sqrt{\frac{\lambda_3(1-\lambda_1)}{\lambda_3-\lambda_1}}\,\mathbf{e}_1 + (-1)^i\sqrt{\frac{\lambda_1(\lambda_3-1)}{\lambda_3-\lambda_1}}\,\mathbf{e}_3\right)\,, \tag{1.30a}$$

$$\mathbf{n}_i = \frac{\sqrt{\lambda_3}-\sqrt{\lambda_1}}{\rho\sqrt{\lambda_3-\lambda_1}}\left(-\sqrt{1-\lambda_1}\,\mathbf{U}_a\mathbf{e}_1 + (-1)^i\sqrt{\lambda_3-1}\,\mathbf{U}_a\mathbf{e}_3\right)\,. \tag{1.30b}$$

Here $\mathbf{e}_j$ are eigenvectors corresponding to the eigenvalues λ_j and ρ is a normalising constant for vector $\mathbf{n}$. Matrices $\widetilde{\mathbf{R}}_1$ and $\widetilde{\mathbf{R}}_2$ are determined from (1.27) substituting respective solution.

Recall that every two variants satisfy similarity relation $\mathbf{U}_b = \mathbf{Q}^{\mathrm{T}}\mathbf{U}_a\mathbf{Q}$ for at least one $\mathbf{Q} \in L_A$ (if variants are different, then necessarily $\mathbf{Q} \notin L_M$ holds). If $\mathbf{Q}$ is a 180° rotation, we can introduce the simpler theorem 1.3.2 for such variants (see [10]).

Theorem 1.3.2 (Mallard law)**.** *Let $\mathbf{U}_a$ and $\mathbf{U}_b$ be distinct variants of martensite. Let $\mathbf{Q} \in L_A$ be a 180° rotation such that*

$$\mathbf{U}_b = \mathbf{Q}^{\mathrm{T}}\mathbf{U}_a\mathbf{Q}\,. \tag{1.31}$$

Let $\mathbf{p}$ *be a unit vector defining the axis of the rotation. Then* $\mathbf{U}_a$ *and* $\mathbf{U}_b$ *are compatible and equation* (1.27) *has exactly two solutions:*

$$\mathbf{n}_1 = \mathbf{p}\,, \qquad \widetilde{\mathbf{a}}_1 = 2\left(\frac{\mathbf{U}_b^{-1}\mathbf{p}}{|\mathbf{U}_b^{-1}\mathbf{p}|^2} - \mathbf{U}_b\mathbf{p}\right)\,, \tag{1.32a}$$

$$\mathbf{n}_2 = \frac{2}{\rho}\left(\mathbf{p} - \frac{\mathbf{U}_b^2\mathbf{p}}{|\mathbf{U}_a\mathbf{p}|^2}\right)\,, \qquad \widetilde{\mathbf{a}}_2 = \rho\mathbf{U}_a\mathbf{p}\,, \tag{1.32b}$$

where ρ *is a normalising constant for vector* $\mathbf{n}_2$*. Matrices* $\widetilde{\mathbf{R}}_1$ *and* $\widetilde{\mathbf{R}}_2$ *are determined from* (1.27) *substituting respective solution.*

The theorem says that the loss of a 180° rotational symmetry during the transition from austenite to martensite gives a rise to possibility of a twinning system creation. It also gives all parameters of this system. In the case of transformations from cubic crystal system the 180° rotational symmetry is always lost. Since austenite is cubic in almost all shape memory alloys, it is not needed to use general theorem 1.3.1 too often.

Using the simple theorem 1.3.2 we are able to decide on type of the twinning system immediately. Consider solution (1.32a). The axis $\mathbf{p}$ is a symmetry element of austenite lattice. Hence, normal $\mathbf{n}_1 = \mathbf{p}$ is a lattice direction in austenite. Then the plane determined by this normal is a lattice plane in austenite. Planes and directions are deformed along with the lattice, therefore the interface after the deformation is a lattice plane in martensite. Thus the solution (1.32a) describes type I twinning system.

The case of the second solution (1.32b) is similar. Since $\mathbf{p}$ is a lattice direction in austenite, the $\rho\mathbf{R}_2\mathbf{U}_b\mathbf{p} = \mathbf{R}_2\widetilde{\mathbf{a}}_2 = \mathbf{a}_2$ is a lattice direction in martensite. Then the solution (1.32b) describes twinning system of type II.

Recall that equation (1.27) has none or exactly two solutions. So, if two rotations $\mathbf{Q}_1$ and $\mathbf{Q}_2$ satisfy premisses of the theorem 1.3.2, the obtained solutions must be identical. Since $\mathbf{Q}_1$ and $\mathbf{Q}_2$ are distinct 180° rotations, they must have distinct rotational axes. Thus the type I solution substituting $\mathbf{Q}_1$ has to be equal to the type II solution substituting $\mathbf{Q}_2$ and same case for the second pair of solutions.

The preceding means that the obtained solution is of compound type. Further, at most two such rotations can exist, otherwise it leads to contradiction to the theorem.

1.4 Martensitic Microstructure

The question for this section is what structure of martensite variants and austenite regions appears in material under given temperature and boundary conditions. Introduced theory of Ball and James is in more detail described in [6].

1.4.1 Transformation Energy

We assess the admissibility of particular structure in terms of energy. As a suitable thermodynamic potential the *Helmholtz free energy*—W appears, which equals to the strain energy for the isothermal processes. Since the transition under consideration is "slow", it can be regarded as isothermal.

Free energy and the corresponding free energy density (w) are considered to be functions of temperature θ and Bain matrix $\mathbf{U}$. Further, we suppose that the free energy depends only on lattice parameters and not on the particular arrangement of atoms. Thus, function $w(\theta, \mathbf{U})$ has to respect lattice symmetries.

By applying rotation $\mathbf{Q}$ from the austenite Laue group L_A to the austenite lattice we get the same lattice. Thus free energy of deformations $\mathbf{y}(\mathbf{x})$ and $\widetilde{\mathbf{y}}(\mathbf{x}) = \mathbf{y}(\mathbf{Q}\mathbf{x})$ must equal. If $\mathbf{F}$ and $\mathbf{U}$ are, respectively, gradient and Bain matrix of the deformation $\mathbf{y}$, then $\mathbf{FQ}$ and $\widetilde{\mathbf{U}}$ are corresponding quantities of the deformation $\widetilde{\mathbf{y}}$ (the chain rule for composite function differentiation is used). According to theorem 1.1.1

$$\widetilde{\mathbf{U}} = \sqrt{(\mathbf{FQ})^{\mathrm{T}}(\mathbf{FQ})} = \sqrt{\mathbf{Q}^{\mathrm{T}}\mathbf{F}^{\mathrm{T}}\mathbf{F}\mathbf{Q}} = \mathbf{Q}^{\mathrm{T}}\sqrt{\mathbf{F}^{\mathrm{T}}\mathbf{F}}\,\mathbf{Q} = \mathbf{Q}^{\mathrm{T}}\mathbf{U}\mathbf{Q}\,. \tag{1.33}$$

The last but one equality results from the uniqueness of the square root operator. So the free energy has to satisfy condition:

$$w(\theta, \mathbf{U}) = w(\theta, \mathbf{Q}^{\mathrm{T}}\mathbf{U}\,\mathbf{Q}) \qquad \forall\, \mathbf{Q} \in L_A\,. \tag{1.34}$$

Therefrom and from (1.24) an important fact, that all variants of martensite are energetically equivalent, follows.

More features of the free energy function can be obtained from the principles of thermodynamics. Stable states of the thermodynamical equilibrium correspond to minima of thermodynamic potentials. In section 1.3 it is mentioned that austenite is stable at high temperature, whereas martensite is stable phase at low temperature. Hence, at fixed high temperature the free energy $w(\theta, \mathbf{U})$ has a minimum in $\mathbf{U} = \mathbf{I}$. At fixed low temperature the minima are in $\mathbf{U} = \mathbf{U}_i,\ i = 1, \ldots, n$, where $\mathbf{U}_i$ are different variants of martensite.

Thanks to the continuous dependence of the free energy on temperature there exists a *transformation temperature*[1)]—θ_T—at which

$$w(\theta_T, \mathbf{I}) = w(\theta_T, \mathbf{U}_a) = \cdots = w(\theta_T, \mathbf{U}_n) \tag{1.35}$$

holds.

[1)] This notation is quite misleading, since the transformation temperature is not the temperature at which the transformation starts. Energetic barriers separating minima of the free energy cause hysteretic behaviour of material.

In sum:

$$\begin{aligned} w(\theta,\mathbf{U}) &\geq w(\theta,\mathbf{I}) && \forall\,\theta > \theta_T\,, \\ w(\theta,\mathbf{U}) &\geq w(\theta,\mathbf{I}) = w(\theta,\mathbf{U}_i) && \theta = \theta_T\,, \\ w(\theta,\mathbf{U}) &\geq w(\theta,\mathbf{U}_i) && \forall\,\theta < \theta_T\,, \end{aligned} \tag{1.36}$$

for all admissible Bain matrices $\mathbf{U}$ and for all $i = 1, 2, \ldots, n$, where n is a number of martensite variants.

1.4.2 Model

Here we suppose that every stable structure minimises the free energy of the transformed region. So we are looking for a deformation $\mathbf{y}(\mathbf{x})$ satisfying the boundary conditions and minimising integral

$$W(\theta,\mathbf{y}) = \int_\Omega w(\theta,\mathbf{U}(\mathbf{y}(\mathbf{x})))\,\mathrm{d}\mathbf{x}\,. \tag{1.37}$$

Unfortunately, according to [4] this variational problem has no solution for general boundary conditions. In that case, there exists a finite infimum of function $W(\theta,\cdot)$, which cannot be reached by any deformation $\mathbf{y}$ satisfying boundary conditions. But with admissible deformations it is possible to approach arbitrarily close to that infimum.

For appropriate boundary conditions, the integral (1.37) can be minimised. Thanks to (1.36), the arrangement of minima of function $w(\theta,\cdot)$ is known for each fixed temperature. At the temperature $\theta > \theta_T$ the free energy density is pointwise minimised by identity (i.e. material remains in the reference austenite state).

Let $\theta < \theta_T$. Consider deformation $\mathbf{y}$ such that corresponding gradient $\mathbf{U}(\mathbf{x})$ at every point represents one of the mutually compatible variants of martensite. Since this deformation minimises the integrand, it also minimises the whole integral. But the resulting structure must fit the boundary conditions. Failing which, only the *minimising sequence* of deformations—$\mathbf{y}^{(n)}$—can be constructed. Such sequence satisfies:

$$\inf_{\mathbf{y}} W(\theta,\mathbf{y}) = \lim_{n\to\infty} W(\theta,\mathbf{y}^{(n)})\,, \tag{1.38}$$

where $\mathbf{y}$ and every member of the sequence fulfil given boundary conditions. The meaning of these sequencies is explained later.

1.4.3 Austenite–martensite Interface

Within some certain temperature range the material can stay both in austenite and in martensite (external loading is not considered). That is because of the thermal hysteresis mentioned above. So it may become that after transition one part of crystal

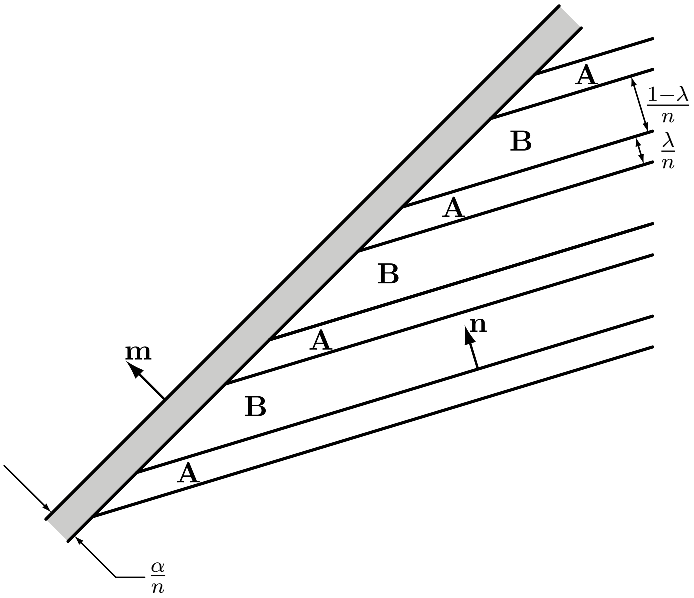

Figure 1.7: Minimising sequence of deformations [6]

transforms to martensite and another rests in austenite. How the interface between these two parts looks like?

If austenite were compatible with martensite, it would be a simple interface like in case of twins. Denote $\mathbf{U}_a$ the particular variant of martensite. Setting $\mathbf{U}_b = \mathbf{I}$ and using theorem 1.3.1 one can see that $\mathbf{U}_a$ is compatible with austenite if and only if the middle eigenvalue of $\mathbf{C} = \mathbf{U}_a^2$ is equal to one. Since Bain matrices are positive definite this condition holds if and only if the middle eigenvalue of the original Bain matrix $\mathbf{U}_a$ is equal to one. But the Bain matrices corresponding to possible martensite variants are determined by lattice parameters. Hence, the ability of forming simple austenite–martensite interfaces strongly depends on the material properties.

An absolute majority of known materials lacks this property.2) Nevertheless, the austenite–martensite interfaces exist also in common materials, but there are not as simple as in the case of direct compatibility between austenite and martensite.

To solve the problem the model from the paragraph 1.4.2 can be used. The part of crystal in martensite is considered as a region Ω. As a boundary condition the deformation gradient $\mathbf{I}$ representing austenite is prescribed. In general, under the given conditions there is no deformation minimising the integral (1.37). But the minimising sequence $\mathbf{y}^{(n)}$ is guaranteed to exist.

Let us construct such sequence. Let $\mathbf{A} = \mathbf{R}_1\mathbf{U}_a$ and $\mathbf{B} = \mathbf{R}_2\mathbf{U}_b$ be suitable,

---

2)It is possible to fabricate materials fulfilling this fine condition. See [11] for details.

compatible martensite variants. Let λ be a such number that convex combination $\lambda\mathbf{A} + (1-\lambda)\mathbf{B}$ is a gradient compatible with austenite. Now

$$\mathbf{A} - \mathbf{B} = \mathbf{a} \otimes \mathbf{n}\,, \tag{1.39a}$$

$$\lambda\mathbf{A} + (1-\lambda)\mathbf{B} - \mathbf{I} = \mathbf{b} \otimes \mathbf{m} \tag{1.39b}$$

holds. Define deformation $\mathbf{y}^{(n)}$ according to Fig. 1.7. Since neither gradient $\mathbf{A}$ nor $\mathbf{B}$ are compatible with austenite, they must be separated from the austenite with *interpolation layer* of width proportional to $\frac{1}{n}$. This layer ensures continuity of the deformation $\mathbf{y}^{(n)}$. Within the interpolation layer the deformation gradient does not correspond to any variant of martensite, so the free energy is not minimised here. The plane with normal $\mathbf{m}$ separating austenite from the twins is called the *habit plane.*

In [6] it is shown that the constructed sequence is a minimising sequence of the integral (1.37). The essential part of this proof is a compatibility of so called *macroscopic gradient* $\lambda\mathbf{A} + (1-\lambda)\mathbf{B}$ and austenite. If it were not for this compatibility, the deformation gradient would diverge in the interpolation layer, and the resulting *macroscopic deformation* would be discontinuous.

Thus, the model allows the infinitely fine laminar structure to arise at the austenite–martensite interface. The volume fraction of one variant in the twining system is λ, and for the second variant it is $1-\lambda$.

Indeed, such fine structures are observed on these interfaces. Of course, the real laminates are not infinitely fine, but this simple model cannot catch the length scale.[3)] The obtained fine system of interfaces is called the *martensitic microstructure.* For an example of microstructure see Fig. 1.8, where the austenite–martensite interface is shown.

Let us return to equation (1.39b). For two compatible martensite variants the number λ and the vectors $\mathbf{b}$, $\mathbf{m}$ solving equation (1.39a) are supposed to exist. But it is possible to find them for all combinations of martensite variants? Can every two variants form simple laminar microstructure on the austenite–martensite interface? Answers are given by following theorem.

Theorem 1.4.1 (Ball, James)**.** *Let* $\mathbf{U}_a$*,* $\mathbf{U}_b$ *be two different variants of martensite, and let* $(\widetilde{\mathbf{R}}, \widetilde{\mathbf{a}}, \mathbf{n})$ *be a solution of equation* (1.27)*. Denote*

$$\delta = \widetilde{\mathbf{a}}\cdot\mathbf{U}_b(\mathbf{U}_b^2 - \mathbf{I})^{-1}\mathbf{n} \quad \textit{and} \quad \eta = \operatorname{tr}\mathbf{U}_b^2 - \det\mathbf{U}_b^2 - 2 + \frac{|\widetilde{\mathbf{a}}|^2}{2\delta}\,. \tag{1.40}$$

[3)] This can be corrected by adding an additional term to integral (1.37) representing “interfacial energy” depending on number of interfaces and their surface area. Such modified model is often in agreement with experimental results, but it is difficult to handle. The simple model presented in this work is sufficient for investigation of basic properties of martensitic microstructures.

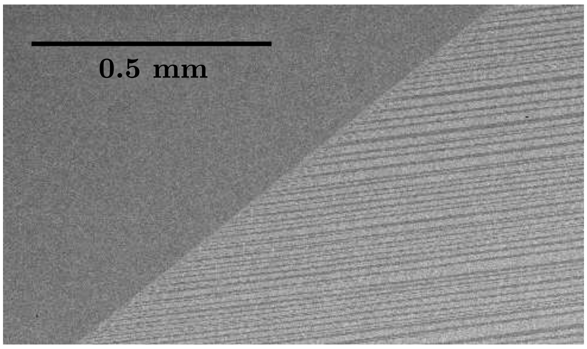

Figure 1.8: Austenite–martensite interface (Cu-Al-Ni alloy, scanning electron microscopy. Photo by DMAT FNSPE.)

Equation

$$\mathbf{Q}(\lambda\widetilde{\mathbf{R}}\mathbf{U}_a + (1-\lambda)\mathbf{U}_b) - \mathbf{I} = \mathbf{b}\otimes\mathbf{m} \tag{1.41}$$

has a solution if and only if

$$\delta \leq -2 \quad \textit{and} \quad \eta \geq 0\,. \tag{1.42}$$

If the condition above is satisfied, then

$$\lambda = \frac{1}{2}\left(1 - \sqrt{1+\frac{2}{\delta}}\right)\,. \tag{1.43}$$

Further denote

$$\mathbf{C} = (\mathbf{U}_b + \lambda\mathbf{n}\otimes\widetilde{\mathbf{a}})\,(\mathbf{U}_b + \lambda\widetilde{\mathbf{a}}\otimes\mathbf{n}) \tag{1.44}$$

and $\lambda_1 \leq \lambda_2 \leq \lambda_3$ *the eigenvalues of matrix* $\mathbf{C}$. *The equation* (1.41) *has exactly two solutions* $(\mathbf{Q}_1, \mathbf{b}_1, \mathbf{m}_1)$ *and* $(\mathbf{Q}_2, \mathbf{b}_2, \mathbf{m}_2)$*:*

$$\mathbf{b}_i = \rho\left(\sqrt{\frac{\lambda_3(1-\lambda_1)}{\lambda_3-\lambda_1}}\,\mathbf{e}_1 + (-1)^i\sqrt{\frac{\lambda_1(\lambda_3-1)}{\lambda_3-\lambda_1}}\,\mathbf{e}_3\right)\,, \tag{1.45a}$$

$$\mathbf{m}_i = \frac{\sqrt{\lambda_3}-\sqrt{\lambda_1}}{\rho\sqrt{\lambda_3-\lambda_1}}\left(-\sqrt{1-\lambda_1}\,\mathbf{e}_1 + (-1)^i\sqrt{\lambda_3-1}\,\mathbf{e}_3\right)\,. \tag{1.45b}$$

Here $\mathbf{e}_j$ *are eigenvectors corresponding to the eigenvalues* λ_j *and* ρ *is a normalising constant for vector* $\mathbf{m}$. *Matrices* $\mathbf{Q}_1$ *and* $\mathbf{Q}_2$ *are determined from* (1.41) *substituting respective solution.*

If $\delta < -2$, *the second pair of solutions is obtained substituting* $1-\lambda$ *for* λ.

Relations between equations (1.26), (1.41) and equations (1.39) are clear:

$$\mathbf{A} = \mathbf{Q}\widetilde{\mathbf{R}}\mathbf{U}_a\,, \tag{1.46a}$$

$$\mathbf{B} = \mathbf{Q}\mathbf{U}_b\,, \tag{1.46b}$$

$$\mathbf{a} = \mathbf{Q}\widetilde{\mathbf{a}}\,. \tag{1.46c}$$

Thus, two suitable variants of martensite can form up to eight different microstructures of type from Fig. 1.8. For each of two solutions of equation (1.27) the four solutions of (1.41) are obtained via the theorem 1.4.1. So, up to eight solutions of system (1.39) can be found.

The same process can be used to construct even much more complicated microstructures (or, more precisely, minimising sequencies). In [6] it is shown that necessary and sufficient condition for sequence of deformations to be a minimising sequence of integral (1.37) is the compatibility of respective macroscopic gradients. Of course, outside interpolation layers the gradients are supposed to be pointwise minimisers of the free energy (i.e. these gradients must correspond to austenite or to martensite variants). Several examples of microstructures are thoroughly analysed in [10].

1.5 Martensitic Transition in CuAlNi

We deal with the microstructures in copper–(14.3%)aluminium–(4.2%)nickel (CuAlNi) single crystal. Thus, let us investigate the martensitic transition in CuAlNi more closely using the theory introduced in previous sections.

1.5.1 Symmetries, Variants of Martensite

During the transition, the cubic lattice of austenite transforms into the orthorhombic lattice of martensite. Cubic primitive unit cell of the austenite lattice changes to tetragonal prism with a rhombic base.

But this prism does not reflect all symmetries of the orthorhombic lattice. Thus, as a conventional unit cell of the martensitic lattice a base-centered cell with the shape of a rectangular parallelepiped is used. The edges of the base of the parallelepiped correspond to the diagonals of the four rhombi lying side by side. See the illustration in Fig. 1.9.

The austenite state is chosen to be a reference configuration. The axes of the coordinate system are aligned with the edges of austenite primitive unit cell. In this

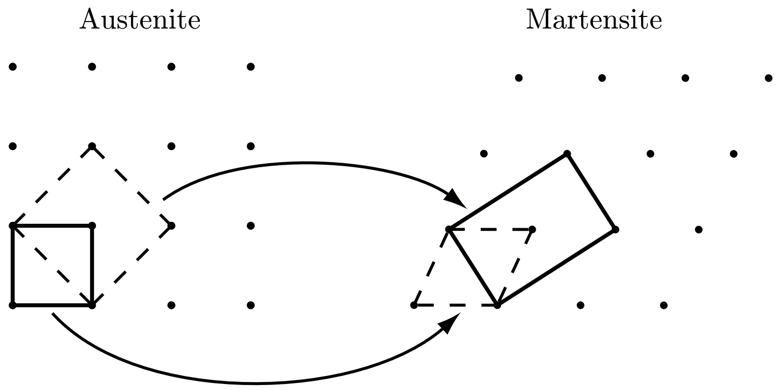

Figure 1.9: Conventional unit cell (full line) in austenite and martensite

configuration, the Bain matrix of the first martensite variant can be written as

$$\mathbf{U} = \begin{pmatrix} E_b & 0 & 0 \\ 0 & E_d & -E_s \\ 0 & -E_s & E_d \end{pmatrix}, \tag{1.47}$$

where E_b, E_d, and E_s are three material constants:

$$E_b = 0.91542\,, \quad E_d = 1.04370\,, \quad E_s = 0.02002\,. \tag{1.48}$$

The cubic lattice Laue group consists of 24 elements, while the Laue group of orthorhombic lattice comprises only 4 elements (identity and three 180° rotations). According to (1.25) six variants of martensite exist in CuAlNi. Bain matrices for all possible variants are obtained using (1.47) and (1.24). We are following the numbering from [18]:

$$\mathbf{U}_1 = \begin{pmatrix} E_b & 0 & 0 \\ 0 & E_d & -E_s \\ 0 & -E_s & E_d \end{pmatrix}, \qquad \mathbf{U}_2 = \begin{pmatrix} E_b & 0 & 0 \\ 0 & E_d & E_s \\ 0 & E_s & E_d \end{pmatrix},$$

$$\mathbf{U}_3 = \begin{pmatrix} E_d & 0 & -E_s \\ 0 & E_b & 0 \\ -E_s & 0 & E_d \end{pmatrix}, \qquad \mathbf{U}_4 = \begin{pmatrix} E_d & 0 & E_s \\ 0 & E_b & 0 \\ E_s & 0 & E_d \end{pmatrix}, \tag{1.49}$$

$$\mathbf{U}_5 = \begin{pmatrix} E_d & -E_s & 0 \\ -E_s & E_d & 0 \\ 0 & 0 & E_b \end{pmatrix}, \qquad \mathbf{U}_6 = \begin{pmatrix} E_d & E_s & 0 \\ E_s & E_d & 0 \\ 0 & 0 & E_b \end{pmatrix}.$$

rot.	$\mathbf{Q}_{A9}$	$\mathbf{Q}_{A10}$	$\mathbf{Q}_{A11}$	$\mathbf{Q}_{A12}$	$\mathbf{Q}_{A13}$	$\mathbf{Q}_{A14}$	$\mathbf{Q}_{A15}$	$\mathbf{Q}_{A16}$	$\mathbf{Q}_{A17}$
axis	$i_1 + i_2$	$i_1 - i_2$	$i_1 + i_3$	$i_1 - i_3$	$i_3 + i_2$	$i_3 - i_2$	i_1	i_2	i_3

Table 1.1: 180° rotations in Laue group of the cubic lattice. Here, i_1, i_2, and i_3 denote standard basis vectors.

$\mathbf{U}_b \diagdown \mathbf{U}_a$	$\mathbf{U}_1$	$\mathbf{U}_2$	$\mathbf{U}_3$	$\mathbf{U}_4$	$\mathbf{U}_5$	$\mathbf{U}_6$
$\mathbf{U}_1$	–	$\mathbf{Q}_{A16}$, $\mathbf{Q}_{A17}$	$\mathbf{Q}_{A10}$	$\mathbf{Q}_{A9}$	$\mathbf{Q}_{A12}$	$\mathbf{Q}_{A11}$
$\mathbf{U}_2$		–	$\mathbf{Q}_{A9}$	$\mathbf{Q}_{A10}$	$\mathbf{Q}_{A11}$	$\mathbf{Q}_{A12}$
$\mathbf{U}_3$			–	$\mathbf{Q}_{A15}$, $\mathbf{Q}_{A17}$	$\mathbf{Q}_{A14}$	$\mathbf{Q}_{A13}$
$\mathbf{U}_4$				–	$\mathbf{Q}_{A13}$	$\mathbf{Q}_{A14}$
$\mathbf{U}_5$					–	$\mathbf{Q}_{A15}$, $\mathbf{Q}_{A16}$
$\mathbf{U}_6$						–

Table 1.2: Rotations satisfying premises of theorem 1.3.2 for variants $\mathbf{U}_a$ and $\mathbf{U}_b$

Further, the list of 180° rotations comprised in austenite Laue group becomes useful. See the listing in Tab. 1.1. These rotations maps one martensite variant to another according to (1.31). The numbering is borrowed from [10].

1.5.2 Twinning Systems

Tab. 1.2 describes relations between 180° rotations listed above and the martensite variants. For variants $\mathbf{U}_a$ and $\mathbf{U}_b$ the rotation $\mathbf{Q}$ from the table satisfies the similarity condition $\mathbf{U}_b = \mathbf{Q}^{\mathrm{T}} \mathbf{U}_a \mathbf{Q}$.

Since for every two variants there is a rotation fulfilling the condition, the theorem 1.3.2 can be used to describe all possible twinning systems in CuAlNi.

Tab. 1.2 and theorem 1.3.2 imply that every two variants are compatible and can create a twinning system. For pairs $\mathbf{U}_1 : \mathbf{U}_2$, $\mathbf{U}_3 : \mathbf{U}_4$, and $\mathbf{U}_5 : \mathbf{U}_6$ there exist two distinct rotations mapping the variants one to another, thus this pairs form twinning systems of the compound type. All other combinations can create either the type I or type II system depending on chosen solution from the theorem.

Altogether, 30 distinct twinning systems exist in CuAlNi (12 systems of type I, 12 systems of type II, and 6 systems of the compound type).

1.5.3 Austenite–martensite Interface

In 1.4.3 it is shown that simple interface between austenite and single variant martensite is admissible if and only if the middle eigenvalue of the corresponding Bain matrix is equal to one. But that is not true in CuAlNi. For the given material the eigenvalues are $\lambda_1 = 0.91542$, $\lambda_2 = 1.02368$, and $\lambda_3 = 1.06372$. The eigenvalues are the same for all variants of martensite due to the similarity of the Bain matrices.

In such case, the second simplest interface allowed by the model is a simple laminar structure showed in Fig. 1.7. This structure can be composed of any two variants creating a twinning system satisfying conditions (1.42). Then the theorem 1.4.1 gives all parameters of such structure (volume fractions of individual variants, orientation of variants with respect to austenite, and habit plane orientation).

By applying theorem 1.4.1 to all possible combinations of martensite variants we found out that the twinning systems of the compound type cannot form such austenite–martensite interface. For arbitrary system of type I or type II the theorem gives four distinct solutions to the compatibility equation (1.41). Thus there are $24 \times 4 = 96$ possible austenite–martensite interfaces from Fig. 1.7 in CuAlNi.

In this thesis we will use the following simple notation for these interfaces. Every interface is identified by five integers (A, B, C, D, E). The first two numbers $(A$, $B)$ stand for the martensite variants involved and they range from 1 to 6. The other numbers equal either 1 or 2. Number C identifies solution from the theorem 1.3.2, thus it identifies the twinning system type ($C = 1$ for type I and $C = 2$ for type II). The fourth number D determines a volume fraction of the variant $\mathbf{U}_A$ (if the volume fraction is less than 0.5, then $D = 1$, $D = 2$ otherwise). The last number E refers to a solution number in theorem 1.4.1.

There is a little ambiguity in the notation since the martensite variants numbers can be swapped. So one physical interface can be described by two different quintuples.

For example, the austenite–martensite interface comprising the type II twinning system of variants $\mathbf{U}_1$ with volume fraction λ and $\mathbf{U}_3$ with volume fraction $1 - \lambda$ corresponding to the second solution from the theorem 1.4.1 is denoted as $(1, 3, 2, 1, 2)$. It can be also denoted as $(3, 1, 2, 2, 2)$, however.

Chapter 2

Analysis and Modelling of Incompatible Microstructures

In the first section of this chapter the introduced classical theory of the reversible martensitic phase transition is applied to analyse compatibility and to identify martensite variants involved in two particular types of microstructure observed experimentally in CuAlNi single crystal. It is shown that so called *lambda* and *X microstructure* (first reported in [5]) do not satisfy premises of the classical theory exactly. Thus, in the next section a little modification to the classical theory is proposed and the whole procedure of incompatible microstructures analysis according to the new theory is developed. The last section focuses on microstructure mobility and the model of observed microstructures evolution is presented here.

2.1 Analysis of the Lambda and X Microstructures

Both microstructures were observed on the same specimen of CuAlNi single crystal. And both microstructures were induced into the specimen by the same experimental procedure. First, the specimen was forced to transform to the single variant martensite by applying uniaxial compression. After removing the compression the specimen stayed in martensite. In the corner of the specimen a small austenite phase nucleus was induced by strong localised heating. Then the whole specimen was heated at the stress-free state. The transition front formed and started moving through the specimen. When the specimen was cooled down, the transition front stopped moving and the microstructure at the interface between austenite and single variant martensite was observed. For the detailed description of the experiment see [20].

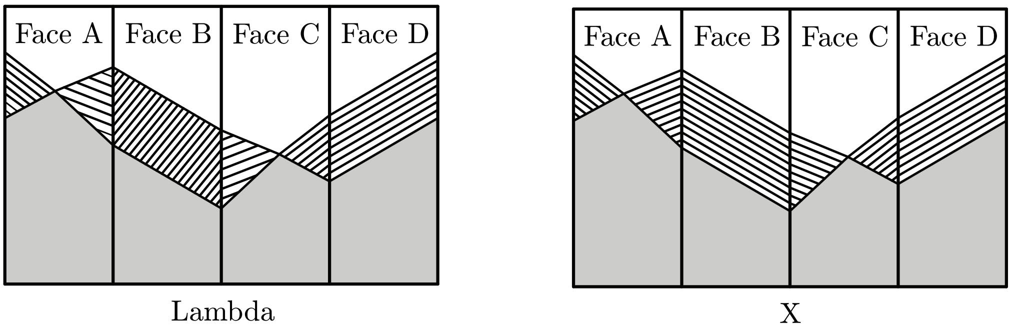

Figure 2.1: Lambda and X microstructures

face	face normal	dimensions [mm]
A, C	$(-0.7218702 \quad -0.6919781 \quad -0.0083517)$	15.07×4.70
B, D	$(0.6918220 \quad -0.7220554 \quad -0.0042752)$	15.07×4.56

Table 2.1: Specimen parameters in austenite

The specimen is a rectangular parallelepiped. For the face normal orientations and dimensions see table Tab. 2.1. The simple illustration of the microstructures and the face naming convention can be seen in Fig. 2.1.

The X microstructure and the lambda microstructure are very similar. Both have a shape of the letter X and consist of two mutually intersecting habit planes separating austenite from twinned regions of martensite (see 1.4.3) and another pair of mutually intersecting interfaces separating these twinned regions from the single variant of martensite.

The lambda microstructure differs from the X microstructure in one of the interfaces between twinned martensite and single variant martensite. Whereas in the case of the X microstructure both martensite–twinned martensite interfaces are parallel (or almost parallel) to the twinning planes of corresponding twinned regions, in the lambda microstructure one of the martensite–twinned martensite interfaces is not. Thus, in the lambda microstructure there is a interface between twinned martensite and single variant martensite, which is similar to a common austenite–martensite interface from Fig. 1.7.

2.1.1 The Lambda Microstructure

The lambda microstructure separating the austenite region from the single variant martensite region is sketched in Fig. 2.2. Four variants of martensite denoted as **A**, **B**, **C**, and **D** are involved. The interface between the {**A**:**B**} twinning system and

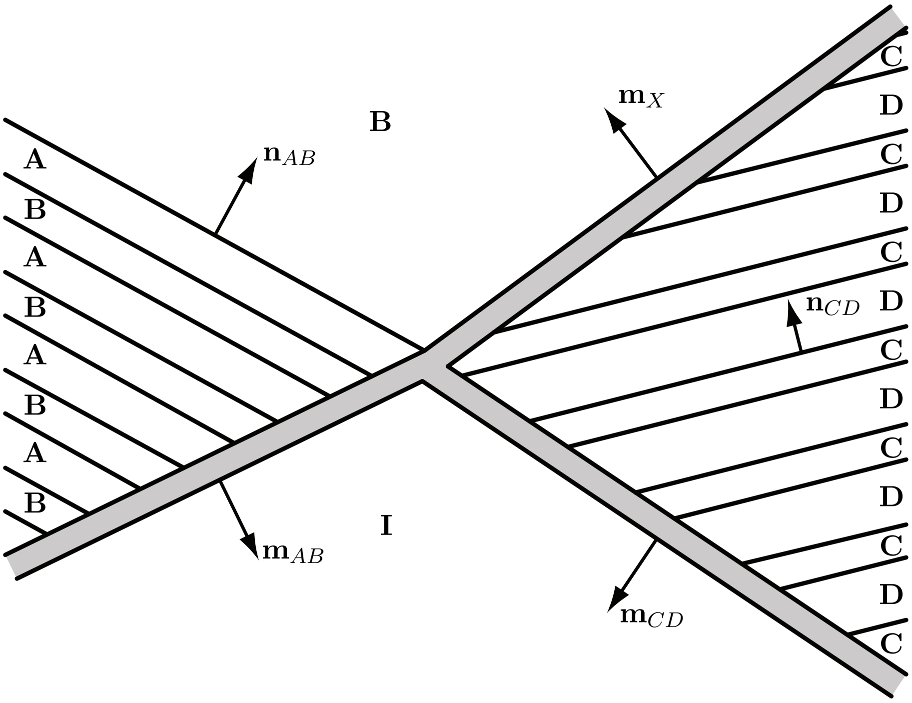

Figure 2.2: Lambda microstructure

single variant **B** is a simple twinning plane. The other three interfaces comprise the interpolation layer introduced in 1.4.3.

Compatibility Equations

With the notation taken from the Fig. 2.2 the compatibility equations (1.41) can be directly rewritten for the {**A**:**B**}:**I** and {**C**:**D**}:**I** habit planes:

$$\begin{aligned} \mathbf{A}-\mathbf{B} &= \mathbf{a}_{AB}\otimes\mathbf{n}_{AB}\,, \\ \lambda_{AB}\mathbf{A}+(1-\lambda_{AB})\mathbf{B}-\mathbf{I} &= \mathbf{b}_{AB}\otimes\mathbf{m}_{AB}\,, \\ \mathbf{C}-\mathbf{D} &= \mathbf{a}_{CD}\otimes\mathbf{n}_{CD}\,, \\ \lambda_{CD}\mathbf{C}+(1-\lambda_{CD})\mathbf{D}-\mathbf{I} &= \mathbf{b}_{CD}\otimes\mathbf{m}_{CD}\,. \end{aligned} \tag{2.1}$$

As mentioned above, the {**A**:**B**}:**B** interface is a simple twinning plane, therefore the compatibility at this interface is ensured by the first equation in (2.1). The compatibility condition for the remaining interface {**C**:**D**}:**B** can be derived following the scheme for ordinary habit plane:

$$\lambda_{CD}\mathbf{C}+(1-\lambda_{CD})\mathbf{D}-\mathbf{B} = \mathbf{b}_X\otimes\mathbf{m}_X\,. \tag{2.2}$$

Using relations (1.46) the conditions (2.1) and (2.2) can be rewritten in the form used in the theorems 1.3.2 and 1.4.1:

$$\begin{aligned} \mathbf{R}_{AB}\mathbf{U}_A - \mathbf{U}_B &= \widetilde{\mathbf{a}}_{AB} \otimes \mathbf{n}_{AB} \,, \\ \mathbf{Q}_{AB}(\lambda_{AB}\mathbf{R}_{AB}\mathbf{U}_A + (1-\lambda_{AB})\mathbf{U}_B) - \mathbf{I} &= \mathbf{b}_{AB} \otimes \mathbf{m}_{AB} \,, \\ \mathbf{R}_{CD}\mathbf{U}_C - \mathbf{U}_D &= \widetilde{\mathbf{a}}_{CD} \otimes \mathbf{n}_{CD} \,, \\ \mathbf{Q}_{CD}(\lambda_{CD}\mathbf{R}_{CD}\mathbf{U}_C + (1-\lambda_{CD})\mathbf{U}_D) - \mathbf{I} &= \mathbf{b}_{CD} \otimes \mathbf{m}_{CD} \end{aligned} \tag{2.3}$$

and

$$\mathbf{Q}_{CD}(\lambda_{CD}\mathbf{R}_{CD}\mathbf{U}_C + (1-\lambda_{CD})\mathbf{U}_D) - \mathbf{Q}_{AB}\mathbf{U}_B = \mathbf{b}_X \otimes \mathbf{m}_X \,. \tag{2.4}$$

The first two and the second two equations in (2.3) are coupled only through the equation (2.4). Thus, for given variants $\mathbf{U}_A$, $\mathbf{U}_B$, $\mathbf{U}_C$, and $\mathbf{U}_D$ all solutions of (2.3) can be easily found by solving them separately using theorem 1.4.1. Then, the solutions of the whole system of equations (2.3) and (2.4) are obtained as solutions of (2.3) that also satisfies (2.4). It was checked that there are no such solutions for any combination of martensite variants.

We found out that the macroscopic deformation gradients in the lambda microstructure cannot be compatible and so that it should not exist according to the classical theory. Since the lambda microstructure is experimentally observed we suppose that the incompatibility is “small”. To prove this assumption we need some tool for measuring the incompatibility of two deformation gradients and to predict the orientation of the interface between these gradients.

Measuring the Gradient Incompatibility

First, the incompatibility measure of two deformation gradients over the given plane is defined. Then, the interface is supposed to be a plane of minimal incompatibility measure. Finally, the incompatibility measure of two gradients is defined as the incompatibility measure over this plane. Precise definitions follow.

Let $\mathbf{F}$ and $\mathbf{G}$ be two deformation gradients and let $\mathcal{T}$ be a plane with normal $\mathbf{n}$. Then, the *incompatibility measure of gradients* $\mathbf{F}$ *and* $\mathbf{G}$ *over the plane* $\mathcal{T}$ is defined as

$$\sup_{\substack{|\mathbf{t}|=1 \\ \mathbf{t}\perp\mathbf{n}}} |\mathbf{F}\mathbf{t} - \mathbf{G}\mathbf{t}| = \sup_{\substack{|\mathbf{t}|=1 \\ \mathbf{t}\in\mathrm{span}(\mathbf{n})^\perp}} |\mathbf{F}\mathbf{t} - \mathbf{G}\mathbf{t}| \,. \tag{2.5}$$

Notice that this value is in fact the operator norm of $(\mathbf{F}-\mathbf{G})_{|\,\mathrm{span}(\mathbf{n})^\perp}$. Obviously, this norm is equal to zero if and only if the gradients are compatible over the plane $\mathcal{T}$ (see 1.1.3).

Then, the *incompatibility measure of* $\mathbf{F}$ *and* $\mathbf{G}$ is

$$\min_{|\mathbf{n}|=1} \|(\mathbf{F}-\mathbf{G})_{|\,\mathrm{span}(\mathbf{n})^{\perp}}\| \,, \tag{2.6}$$

and the *minimal incompatibility plane* is every plane with the normal

$$\mathbf{m} = \arg\min_{|\mathbf{n}|=1} \|(\mathbf{F}-\mathbf{G})_{|\,\mathrm{span}(\mathbf{n})^{\perp}}\| \,. \tag{2.7}$$

The expression (2.7) is easily evaluated using the *singular value decomposition (SVD)* of the matrix $\mathbf{F}-\mathbf{G}$. For details about SVD see [24]. SVD enable us to write

$$\mathbf{F}-\mathbf{G} = \sigma_1\mathbf{a}_1\otimes\mathbf{h}_1 + \sigma_2\mathbf{a}_2\otimes\mathbf{h}_2 + \sigma_3\mathbf{a}_3\otimes\mathbf{h}_3 \,, \tag{2.8}$$

where $\{\mathbf{a}_1,\mathbf{a}_2,\mathbf{a}_3\}$ and $\{\mathbf{h}_1,\mathbf{h}_2,\mathbf{h}_3\}$ are the orthonormal sets and the numbers σ_i are nonnegative, descending. The vectors $\mathbf{h}_i$ are called *the left singular vectors*, the vectors $\mathbf{a}_i$ are *the right singular vectors*, and the numbers σ_i are called *the singular values.*

It is easy to see that

$$(\mathbf{a}\otimes\mathbf{h})\mathbf{v} = \mathbf{a}\mathbf{h}^{\mathrm{T}}\mathbf{v} = \mathbf{a}(\mathbf{h}\cdot\mathbf{v}) \,, \tag{2.9}$$

hence

$$(\mathbf{F}-\mathbf{G})\mathbf{h}_i = \sigma_i\mathbf{a}_i \,. \tag{2.10}$$

So the SVD gives a picture of the matrix action on vectors. The operator norm of the matrix is equal to its largest singular value—σ_1. It can be also seen from (2.9) that $\mathbf{a}_i\otimes\mathbf{h}_i$ is a rank-one matrix with the kernel $\mathrm{span}(\mathbf{h}_i)^{\perp}$ and range $\mathrm{span}(\mathbf{a}_i)$.

Now, it should be clear that the minimal incompatibility plane we are looking for is the kernel of $\sigma_1\mathbf{a}_1\otimes\mathbf{h}_1$, or more precisely, every plane with the normal $\mathbf{h}_1$. Because this is the plane, where the largest singular value σ_1 is "inactive".

The operator norm of the restriction $(\mathbf{F}-\mathbf{G})_{|\,\mathrm{span}(\mathbf{h}_1)^{\perp}}$ and the sought incompatibility measure is the second largest singular value – σ_2. In sum:

$$\mathbf{m} = \arg\min_{|\mathbf{n}|=1} \|(\mathbf{F}-\mathbf{G})_{|\,\mathrm{span}(\mathbf{n})^{\perp}}\| = \mathbf{h}_1 \quad \text{and} \tag{2.11}$$

$$\sup_{\substack{|\mathbf{t}|=1\\ \mathbf{t}\in\mathrm{span}(\mathbf{n})^{\perp}}} |\mathbf{F}\mathbf{t}-\mathbf{G}\mathbf{t}| = \|(\mathbf{F}-\mathbf{G})_{|\,\mathrm{span}(\mathbf{n})^{\perp}}\| = \sigma_2 \,. \tag{2.12}$$

This approach is a generalisation into 3D of the "misfit" defined in the work [21] for the 2D case. In 2D the situation is much more simpler, because the interface is a one-dimensional line, and thus there is no need for searching for supremum in (2.5).

angle $\diagdown$ *face*	**A**	**B**	**C**
$(\mathbf{m}_{AB}, \mathbf{n}_{CD})$	50.1°		48.4°
$(\mathbf{m}_{AB}, \mathbf{m}_{X})$	17.5°		17.8°
$(\mathbf{m}_{AB}, \mathbf{m}_{CD})$	54.8°		55.8°
$(\mathbf{n}_{AB}, \mathbf{n}_{CD})$	4.1°		1.8°
$(\mathbf{n}_{AB}, \mathbf{m}_{CD})$	9.7°		7.8°
$(\mathbf{n}_{AB}, \mathbf{m}_{X})$	63.6°		64.6°
$(\mathbf{m}_{AB}, \mathbf{n}_{AB})$	46.2°		47.5°
$(\mathbf{m}_{CD}, \mathbf{n}_{CD})$	5.6°	85.2°	5.3°
$(\mathbf{m}_{CD}, \mathbf{m}_{X})$	72.7°	2.2°	72.4°
$(\mathbf{n}_{CD}, \mathbf{m}_{X})$	68.0°	80.6°	66.7°
$(\mathbf{m}_{AB}, \text{edge})$	67.8°		67.5°
$(\mathbf{n}_{AB}, \text{edge})$	66.6°		66.7°
$(\mathbf{m}_{CD}, \text{edge})$	55.5°	45.4°	57.6°
$(\mathbf{n}_{CD}, \text{edge})$	63.0°	51.6°	63.8°
$(\mathbf{m}_{X}, \text{edge})$	49.6°	47.5°	50.2°

Table 2.2: The angles measured on the lambda microstructure

Identification of Martensite Variants

To identify the variants of martensite involved in the lambda microstructure we compare the lambda microstructure geometry defined by the interfaces orientation obtained from the compatibility equations with the experimentally observed geometry. It is supposed that for the sought set of variants the theoretically predicted geometry best fits the observed microstructure.

Since there are no exact solutions of the all compatibility equations (2.3) and (2.4) for the lambda interface, we are looking for solutions of (2.3) only with the minimal incompatibility of the deformation gradient $\mathbf{B}$ and the macroscopic deformation gradient of the $\{\mathbf{C}:\mathbf{D}\}$ twinning system.

For the purpose of the geometry comparison mentioned above the angles between visible interfaces in the particular faces of the specimen were measured. The obtained data summarises Tab. 2.2. We denote $(\mathbf{m}, \mathbf{n})_A$ the angle between the planes with normals $\mathbf{m}$ and $\mathbf{n}$ projected into the face A. In the table the index of the face is omitted. If there is a word "edge" in the place of the second normal, the notation means the angle between the longer edge of the specimen and the intersection line of the plane determined by the first normal and the given face.

In backtracking algorithm the angles $(\mathbf{m}_{AB}, \mathbf{m}_{CD})_C$, $(\mathbf{m}_{AB}, \mathbf{n}_{CD})_C$, $(\mathbf{m}_{AB}, \mathbf{n}_{AB})_C$, $(\mathbf{m}_{CD}, \mathbf{n}_{CD})_C$, and $(\mathbf{m}_{CD}, \mathbf{n}_{CD})_B$ were compared against observation for all solutions of (2.3) for all combinations of martensite variants. Within 5° tolerance only one solution describing the lambda microstructure with incompatibility over the $\{\mathbf{C}:\mathbf{D}\}:\mathbf{B}$

angle $\diagdown$ *face*	**A**	**B**	**C**
$\Delta(\mathbf{m}_{AB}, \mathbf{n}_{CD})$	$-2.7°$		$-0.9°$
$\Delta(\mathbf{m}_{AB}, \mathbf{m}_{X})$	$0.9°$		$0.6°$
$\Delta(\mathbf{m}_{AB}, \mathbf{m}_{CD})$	$-2.5°$		$-3.5°$
$\Delta(\mathbf{n}_{AB}, \mathbf{n}_{CD})$	$-1.2°$		$1.1°$
$\Delta(\mathbf{n}_{AB}, \mathbf{m}_{CD})$	$-1.9°$		$-0.0°$
$\Delta(\mathbf{n}_{AB}, \mathbf{m}_{X})$	$-0.6°$		$-1.6°$
$\Delta(\mathbf{m}_{AB}, \mathbf{n}_{AB})$	$-1.6°$		$-2.9°$
$\Delta(\mathbf{m}_{CD}, \mathbf{n}_{CD})$	$-0.7°$	$-3.7°$	$-0.4°$
$\Delta(\mathbf{m}_{CD}, \mathbf{m}_{X})$	$-1.9°$	$0.3°$	$-1.6°$
$\Delta(\mathbf{n}_{CD}, \mathbf{m}_{X})$	$-2.1°$	$-1.6°$	$-0.8°$
$\Delta(\mathbf{m}_{AB}, \text{edge})$	$0.9°$		$1.2°$
$\Delta(\mathbf{n}_{AB}, \text{edge})$	$0.1°$		$-0.0°$
$\Delta(\mathbf{m}_{CD}, \text{edge})$	$3.4°$	$1.1°$	$1.3°$
$\Delta(\mathbf{n}_{CD}, \text{edge})$	$0.8°$	$0.4°$	$0.0°$
$\Delta(\mathbf{m}_{X}, \text{edge})$	$0.7°$	$1.5°$	$0.1°$

Table 2.3: Differences between the theoretically predicted and measured angles for the lambda microstructure

interface less than 0.01 was found. For the other solutions within the given tolerance the incompatibility measure was greater than 0.05.

Results

The $\{\mathbf{A}{:}\mathbf{B}\}{:}\mathbf{I}$ habit plane was identified as $(2, 6, 2, 1, 1)$, and the $\{\mathbf{C}{:}\mathbf{D}\}{:}\mathbf{I}$ habit plane was identified as $(3, 6, 2, 1, 1)$. We are using notation introduced in 1.5.3. Thus, both twinning systems are of the type II. The $\{\mathbf{A}{:}\mathbf{B}\}$ system comprises variants 2 and 6, where the second one is also the variant of the single variant region. The $\{\mathbf{C}{:}\mathbf{D}\}$ twinning system shares the variant 6, the second involved variant is variant number 3. The incompatibility measure over the $\{\mathbf{C}{:}\mathbf{D}\}{:}\mathbf{B}$ interface is 0.0029. In the Tab. 2.3 the differences between the theoretically predicted and measured angles are shown. The normal $\mathbf{m}_X$ is determined from (2.11).

In addition to deformation gradient incompatibility another issue arises. The normal vectors of predicted interfaces are not coplanar, which implies that the predicted interfaces do not intersect in one line and thus they do not form the “X shape” exactly. The situation is clear from the Fig. 2.3.

2.1.2 The X Microstructure

In the Fig. 2.4 the X microstructure is illustrated. It is simpler than the lambda microstructure, since it consists of two ordinary twinning systems bordering austenite

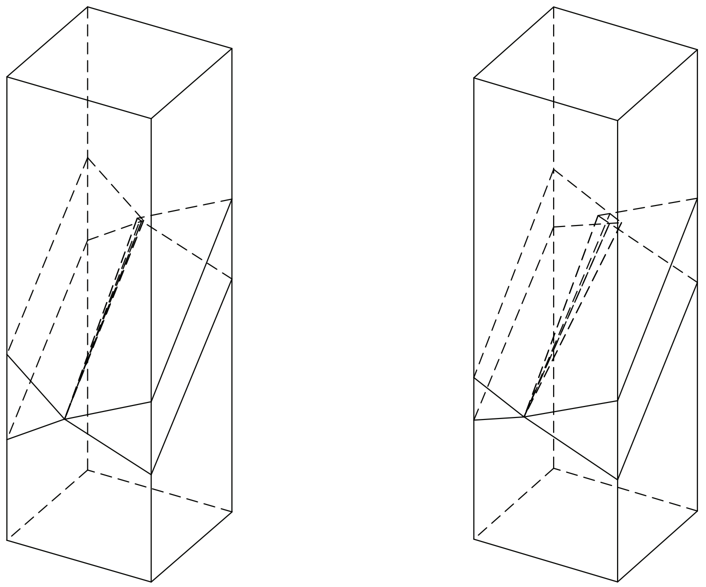

Lambda X

Figure 2.3: The predicted geometry of the lambda and X microstructures (in austenite)

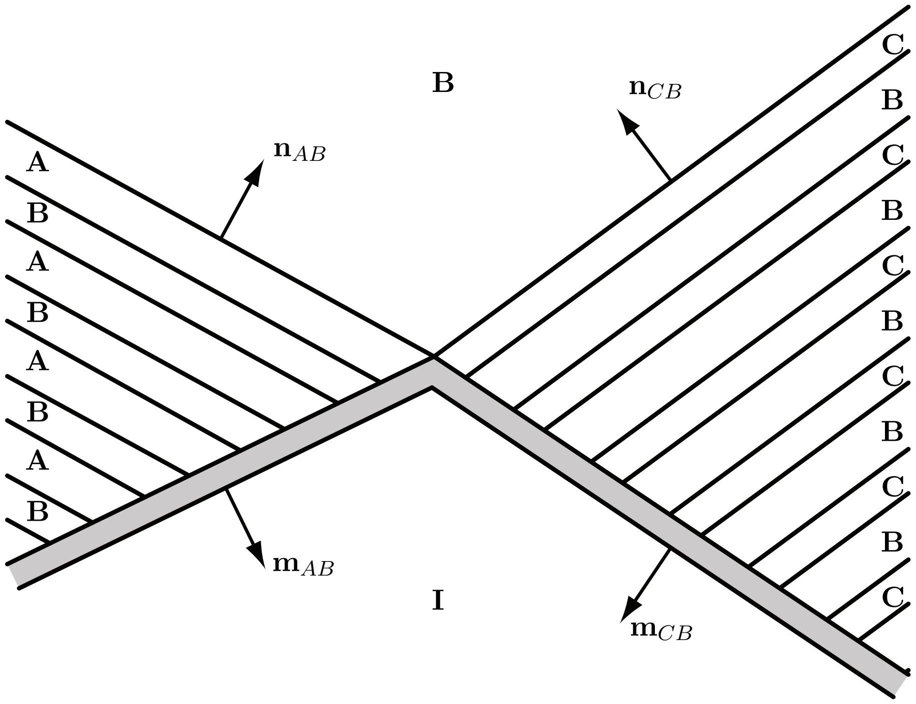

Figure 2.4: X microstructure

through the habit planes and single variant martensite through the simple twinning planes. Thus, it comprises only three variants of martensite **A**, **B**, and **C**.

Compatibility Equations

The compatibility over the martensite–twinned martensite interfaces is guaranteed by the twinning equations. Thus, the compatibility conditions for the X microstructure contains only these twinning equations and pair of equations ensuring compatibility with austenite:

$$\begin{aligned} \mathbf{A} - \mathbf{B} &= \mathbf{a}_{AB} \otimes \mathbf{n}_{AB} \, , \\ \lambda_{AB}\mathbf{A} + (1-\lambda_{AB})\mathbf{B} - \mathbf{I} &= \mathbf{b}_{AB} \otimes \mathbf{m}_{AB} \, , \\ \mathbf{C} - \mathbf{B} &= \mathbf{a}_{CB} \otimes \mathbf{n}_{CB} \, , \\ \lambda_{CB}\mathbf{C} + (1-\lambda_{CB})\mathbf{B} - \mathbf{I} &= \mathbf{b}_{CB} \otimes \mathbf{m}_{CB} \, . \end{aligned} \tag{2.13}$$

Using (1.46) we can write:

$$\begin{aligned} \mathbf{R}_{AB}\mathbf{U}_A - \mathbf{U}_B &= \tilde{\mathbf{a}}_{AB} \otimes \mathbf{n}_{AB} \, , \\ \mathbf{Q}_{AB}(\lambda_{AB}\mathbf{R}_{AB}\mathbf{U}_A + (1-\lambda_{AB})\mathbf{U}_B) - \mathbf{I} &= \mathbf{b}_{AB} \otimes \mathbf{m}_{AB} \, , \\ \mathbf{R}_{CB}\mathbf{U}_C - \mathbf{U}_B &= \tilde{\mathbf{a}}_{CB} \otimes \mathbf{n}_{CB} \, , \\ \mathbf{Q}_{CB}(\lambda_{CB}\mathbf{R}_{CB}\mathbf{U}_B + (1-\lambda_{CB})\mathbf{U}_B) - \mathbf{I} &= \mathbf{b}_{CB} \otimes \mathbf{m}_{CB} \, . \end{aligned} \tag{2.14}$$

Here, the rotations $\mathbf{Q}_{AB}$ and $\mathbf{Q}_{CB}$ coming from the polar decomposition of the same deformation gradient **B** have to equal. But we distinguish them to “decouple” the pairs of equations (2.14). Providing the condition

$$\mathbf{Q}_{AB} = \mathbf{Q}_{CB} \tag{2.15}$$

the same type of the problem as for the lambda microstructure is obtained. First, the equations (2.14) are solved separately using the theorem 1.4.1 and obtained solutions are checked against the condition (2.15). Again, we found out that there is no solution of given system for any combination of martensite variants.

Identification of Martensite Variants

Following the procedure used for the lambda microstructure the variants comprised in the X microstructure were identified. The geometry of the all possible solutions of (2.14) was compared to observations. Fixing $\mathbf{B} = \mathbf{Q}_{AB}\mathbf{U}_B$, the $\{\mathbf{C}{:}\mathbf{B}\}{:}\mathbf{B}$ interface remains the only incompatible interface in the X microstructure. Thus, the solution fitting the observed geometry within given tolerance with the minimal incompatibility over the $\{\mathbf{C}{:}\mathbf{B}\}{:}\mathbf{B}$ interface is chosen.

angle $\diagdown$ *face*	**A**	**B**	**C**	**D**
$(\mathbf{m}_{AB}, \mathbf{n}_{CB})$	2.0°		2.0°	
$(\mathbf{m}_{AB}, \mathbf{m}_{CB})$	44.0°		43.4°	
$(\mathbf{n}_{AB}, \mathbf{n}_{CB})$	49.0°		49.0°	
$(\mathbf{n}_{AB}, \mathbf{m}_{CB})$	3.0°		4.0°	
$(\mathbf{m}_{AB}, \mathbf{n}_{AB})$	47.0°		46.9°	1.3°
$(\mathbf{m}_{CB}, \mathbf{n}_{CB})$	46.0°	0.0°	45.0°	
$(\mathbf{m}_{AB}, \text{edge})$	67.0°		67.0°	48.2°
$(\mathbf{n}_{AB}, \text{edge})$	66.2°		65.5°	47.2°
$(\mathbf{m}_{CB}, \text{edge})$	69.4°	46.5°	68.9°	
$(\mathbf{n}_{CB}, \text{edge})$	65.0°	46.6°	65.0°	

Table 2.4: The angles measured on the X microstructure

angle $\diagdown$ *face*	**A**	**B**	**C**	**D**
$\Delta(\mathbf{m}_{AB}, \mathbf{n}_{CB})$	2.5°		2.5°	
$\Delta(\mathbf{m}_{AB}, \mathbf{m}_{CB})$	−3.3°		−2.7°	
$\Delta(\mathbf{n}_{AB}, \mathbf{n}_{CB})$	0.7°		0.7°	
$\Delta(\mathbf{n}_{AB}, \mathbf{m}_{CB})$	1.5°		0.5°	
$\Delta(\mathbf{m}_{AB}, \mathbf{n}_{AB})$	−1.8°		−1.7°	−0.8°
$\Delta(\mathbf{m}_{CB}, \mathbf{n}_{CB})$	−0.8°	2.1°	0.2°	
$\Delta(\mathbf{m}_{AB}, \text{edge})$	1.0°		1.0°	−0.7°
$\Delta(\mathbf{n}_{AB}, \text{edge})$	0.6°		1.3°	−1.9°
$\Delta(\mathbf{m}_{CB}, \text{edge})$	2.0°	1.0°	2.5°	
$\Delta(\mathbf{n}_{CB}, \text{edge})$	−1.6°	−1.2°	−1.6°	

Table 2.5: Differences between the theoretically predicted and measured angles for the X microstructure

The angles measured on the X interface are listed in the Tab. 2.4. For the comparison with observations, in the backtracking algorithm the angles $(\mathbf{m}_{AB}, \mathbf{m}_{CB})_A$, $(\mathbf{m}_{AB}, \mathbf{n}_{AB})_A$, $(\mathbf{m}_{CB}, \mathbf{n}_{CB})_A$, $(\mathbf{m}_{AB}, \mathbf{n}_{AB})_D$, and $(\mathbf{m}_{CB}, \mathbf{n}_{CB})_B$ were chosen. As was the case of the lambda microstructure, within the 5° tolerance only one solution describing the X microstructure with the incompatibility over the {**C**:**B**}:**B** interface less than 0.01 was found. For the other solutions within the given tolerance the incompatibility measure was greater than 0.05.

Results

The {**A**:**B**}:**I** habit plane was identified as $(2, 6, 2, 1, 1)$ and the {**C**:**B**}:**I** habit plane was identified as $(4, 6, 2, 1, 1)$. Both twinning systems are of the type II. Notice that the habit plane {**A**:**B**}:**I** and the corresponding twinning system are the same as in the case of the lambda microstructure. And again, the common martensite variant is the variant number 6. The incompatibility measure over the {**C**:**B**}:**B** interface is 0.0036. In the Tab. 2.5 the differences between the theoretically predicted and measured angles are shown.

Although the {**C**:**B**}:**B** interface is chosen to be incompatible, instead of the minimal incompatibility plane normal, for simplicity, the twinning plane normal is used for geometry evaluations. Since the angle between these two normals is less than 3° , the accuracy is sufficient for our purposes.

Even in the X microstructure the predicted interfaces do not intersect in one line. See the Fig. 2.3 for the model of the predicted geometry. Since the real interfaces must meet in one line to form the X microstructure, it leads to situation where even compatible regions border over incompatible interface.

2.1.3 Conclusions

It was shown that both microstructures do not fulfil compatibility conditions required by the classical theory introduced in the first chapter. Similar results are presented in [17] for the X microstructure in Indium-Thallium undergoing cubic to tetragonal martensitic transition. It means that the sequences of deformations corresponding to observed microstructures are not the minimising sequences of the integral (1.37). This breaks the main assumption of the introduced theory about the stable microstructures, which, according to this theory, have to be global minimisers of the Helmholtz free energy. This issue will be discussed in detail in the next section 2.2.

Though the microstructures do not satisfy basic premises of the classical theory, the results of this theory were used to identify involved martensite variants. This is possible as the incompatibility of the analysed microstructures is small. We suppose that this small incompatibility is compensated by the presence of elastic strains. Thus, the geometry of the real microstructure does not differ too much from the geometry predicted by the classical theory providing releasing some compatibility conditions. This claim is backed up with data listed in Tab. 2.3 and Tab. 2.5.

2.2 Modified Model of the Martensitic Microstructure

In the previous section we found out that the microstructures under investigation cannot exist without presence of the elastic strains due to geometric incompatibility. Therefore, the corresponding minimising sequences cannot be global minimisers of the stored Helmholtz free energy (1.37).

We propose a slight modification of the classical theory. The stable microstructure is supposed to be only a local minimiser of the stored free energy. Based on the results presented above we suppose that the geometry predicted by the classical theory lies close to the sought local minimum of the total free energy.

To predict the microstructure geometry with the aid of this modified model the local minimum of the total free energy with respect to chosen geometric parameters must be found. This section describes the particular steps of this procedure.

2.2.1 Helmholtz Free Energy Estimation

To evaluate the total free energy of the specimen after the phase transition the whole process is considered to be isothermal. Then, the free energy is totally differentiable with respect to deformation. Thus, it does not depend on the transition path. This property enables us to understand the martensitic transition as two independent processes. The first is an inelastic transformation given by the transition strains which yields to the discontinuous deformation over the incompatible interfaces. The second one is the subsequent elastic deformation which ensures the continuity of the resulting body. Hence, the total free energy A is a sum of the transformation energy W and the free energy of the elastic deformation W_e:

$$A = W + W_e \,. \tag{2.16}$$

The properties of the transformation energy W are summarised in 1.4.1. When the specimen is set at the transition temperature θ_T, the transformation free energy density w does not depend on the phase (see (1.36)). Thus, the transformation energy W is function of specimen volume only and it is independent on the microstructure parameters. Therefore, the total free energy A can be identified with the free energy of the elastic deformation W_e only. For the isothermal case the free energy of the elastic deformation is equal to the stored elastic energy E_e:

$$A = W_e = E_e \,. \tag{2.17}$$

Elastic Deformation Evaluation

Evaluation of the elastic strain fields in a body is a subject of comprehensive general theory of elasticity [14]. Only the basic concept is explained in this text.

To find the elastic strain field in the deformed body we need to know the *elastic constants* C_{ijkl} of the material (the stiffness tensor) and the boundary conditions. The boundary conditions are generally given by the prescribed displacements or applied forces. Then, we can solve the problem of *static equilibrium* of the body for the displacement field $\mathbf{u}(\mathbf{x})$.

The *principle of virtual work* is used to obtain a variational formulation of the problem, which is usually solved by the finite element method (FEM). In the regime of *small deformations (linear elasticity)* the equations to solve are linear.

With the given displacement field the elastic energy E_e of the deformation is defined as:

$$E_e = \frac{1}{2} \int_{\mathcal{V}} C_{ijkl} \varepsilon_{ij} \varepsilon_{kl} \, \mathrm{d}\mathbf{x} \,, \tag{2.18}$$

where the $\mathcal{V}$ denotes deformed volume and ε_{ij} denotes the *infinitesimal strain tensor (Cauchy's strain tensor)*, which is defined by following relation:

$$\varepsilon_{ij} = \frac{1}{2} \left(\frac{\partial u_i}{\partial x_j} + \frac{\partial u_j}{\partial x_i} \right) \,. \tag{2.19}$$

Formulation of the Static Equilibrium Problem

As mentioned above, to obtain elastic strain field involved in the microstructure we need to supply elastic constants of the material and set up the proper boundary conditions. The elastic constants of the austenite and single variant martensite in CuAlNi were measured using ultrasonic methods ([13]). Since we want to avoid strongly multiscale computations, we consider the twinned regions homogeneous transforming according to the corresponding macroscopic gradients. The "average" elastic constants of this regions are obtained using homogenisation procedure described in [13].

To determine the boundary conditions let us sum up the abstract idea of the microstructure creation process. Let the specimen before the transition occupy the simply connected volume Ω. The volume Ω consists of smaller volumes $\mathcal{G}_m$ ($\mathcal{G}_m$ are closed and $\mathcal{G}_m^\circ$ are disjoint), on which the deformations $\mathbf{y}_m(\mathbf{x}) = \mathbf{F}_m\mathbf{x} + \mathbf{b}_m$ are defined. These affine transformations describe the phase transitions of the respective volumes. The macroscopic gradient $\mathbf{F}_m = \mathbf{R}_m\mathbf{U}_m$ is upon the rotation $\mathbf{R}_m$ determined by the material phase (or phase mixture in the case of the twinned regions). Rotations $\mathbf{R}_m$ and the translation vectors $\mathbf{b}_m$ are obtained from the conditions of compatibility with the surrounding volumes. They remain arbitrary, in the case of incompatibility.

In general, the boundaries $\partial\mathcal{G}_m$ are not the compatibility planes, thus, after applying the prescribed deformations, the original volume Ω breaks up into several parts. So, after the transformation we end up with separated volumes $\mathcal{V}_m = \mathbf{y}_m(\mathcal{G}_m)$. Now we are looking for elastic deformation of each volume $\mathcal{V}_m$, which puts these parts back together. More precisely, we are looking for the set of displacement fields $\widetilde{\mathbf{u}}_m(\mathbf{x})$ defined on $\mathcal{V}_m$ such that the composition $\widetilde{\mathbf{y}}$ defined by

$$\widetilde{\mathbf{y}}_{|\mathcal{G}_m} = \mathbf{y}_m + \widetilde{\mathbf{u}}_m \circ \mathbf{y}_m \tag{2.20}$$

is a continuous deformation on the whole Ω.

Now let us define the necessary boundary conditions. Consider adjoining incompatible volumes $\mathcal{G}_m$ and $\mathcal{G}_n$, and denote their common part of boundary $\partial\mathcal{G}_{mn} = \mathcal{G}_m \cap \mathcal{G}_n$. Let $\mathbf{x}$ be a point of $\partial\mathcal{G}_{mn}$, then this point transforms to two different points $\widetilde{\mathbf{x}}_m = \mathbf{y}_m(\mathbf{x})$ and $\widetilde{\mathbf{x}}_n = \mathbf{y}_n(\mathbf{x})$ in the transformed configuration. The requirement on the sought displacement field is that these two points become one after the elastic deformation,

$$\widetilde{\mathbf{x}}_m + \widetilde{\mathbf{u}}_m(\widetilde{\mathbf{x}}_m) = \widetilde{\mathbf{x}}_n + \widetilde{\mathbf{u}}_n(\widetilde{\mathbf{x}}_n)\,. \tag{2.21}$$

The relation between the points $\widetilde{\mathbf{x}}_m$ and $\widetilde{\mathbf{x}}_n$ is clear:

$$\widetilde{\mathbf{x}}_n = (\mathbf{y}_n \circ \mathbf{y}_m^{-1})(\widetilde{\mathbf{x}}_m) = \mathbf{F}_n\mathbf{F}_m^{-1}(\widetilde{\mathbf{x}}_m - \mathbf{b}_m) + \mathbf{b}_n\,. \tag{2.22}$$

Substituting to (2.21) we get

$$\widetilde{\mathbf{x}}_m + \widetilde{\mathbf{u}}_m(\widetilde{\mathbf{x}}_m) = \mathbf{F}_n\mathbf{F}_m^{-1}(\widetilde{\mathbf{x}}_m - \mathbf{b}_m) + \mathbf{b}_n + \widetilde{\mathbf{u}}_n\big(\mathbf{F}_n\mathbf{F}_m^{-1}(\widetilde{\mathbf{x}}_m - \mathbf{b}_m) + \mathbf{b}_n\big)\,. \tag{2.23}$$

The relation above has to hold for an arbitrary $\widetilde{\mathbf{x}}_m \in \partial\mathcal{V}_{mn}$. Thus, the boundary condition for the field $\mathbf{u}_m$ on the boundary part $\partial\mathcal{V}_{mn} = \mathbf{y}_m(\partial\mathcal{G}_{mn})$ can be written as

$$\widetilde{\mathbf{u}}_m(\widetilde{\mathbf{x}}) = \mathbf{F}_n\mathbf{F}_m^{-1}(\widetilde{\mathbf{x}} - \mathbf{b}_m) + \mathbf{b}_n + \widetilde{\mathbf{u}}_n\big(\mathbf{F}_n\mathbf{F}_m^{-1}(\widetilde{\mathbf{x}} - \mathbf{b}_m) + \mathbf{b}_n\big) - \widetilde{\mathbf{x}} \quad \forall\,\widetilde{\mathbf{x}} \in \partial\mathcal{V}_{mn}\,. \tag{2.24}$$

Analogously, the displacements for the other incompatible boundaries are prescribed. Notice that the condition on the boundary part $\partial\mathcal{V}_{mn}$ is equivalent to the condition on the part $\partial\mathcal{V}_{nm}$, hence, it is sufficient to define only one of these.

Besides the known terms $\mathbf{F}_m$, $\mathbf{F}_n$, $\mathbf{b}_m$, and $\mathbf{b}_n$, also the dependent variable $\mathbf{u}_n$ corresponding to different volume $\mathcal{V}_n$ figures in the condition (2.24). Thus, the problem of finding suitable elastic deformation leads to a system of coupled problems of static equilibrium introduced above. The solution is a set of displacement fields $\widetilde{\mathbf{u}}_m(\widetilde{\mathbf{x}})$.

The similar approach was presented in [3] to evaluate the strain fields in the so called *wedge microstructure*, but the geometry of the wedge microstructure is simple. It does not break up after the applying transformation strains, only a gap arises in the body. To “seal” that gap the single problem of static equilibrium must be solved.

2.2.2 Geometry Parametrisation and Optimisation

We are searching for minimum of the total free energy with respect to two material parameters and six geometric parameters. The dimensions of the specimen are fixed as well as the position of the microstructure. All parameters are defined for the X microstructure in the same way as for the lambda microstructure. The first two parameters (λ_1, λ_2) stand for the volume fractions of the common variant in both twinning systems.

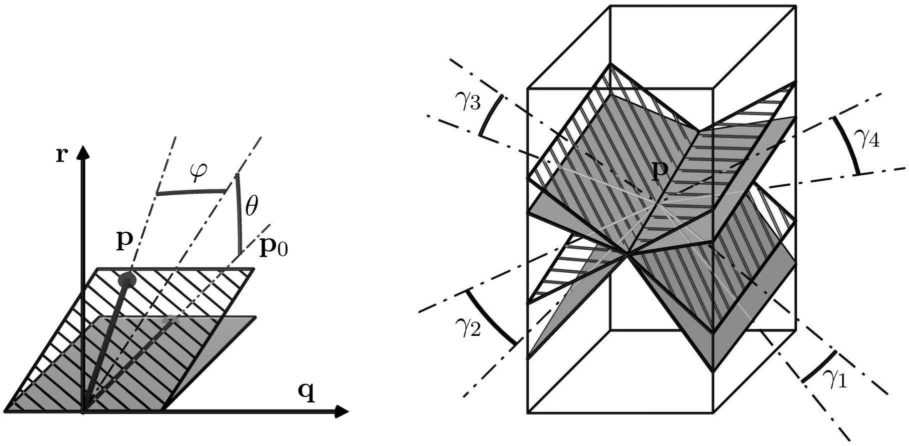

Figure 2.5: Geometric parameters of the microstructures

An important property of the both microstructures is a direction of the intersecting line of all interfaces, since this is not well defined by the predictions of the classical theory. Thus, the second two parameters define the direction of the intersecting line **p**. The direction is given by two angles θ and φ (see Fig. 2.5), which describe the deviation of this line from the direction $\mathbf{p}_0$ of the intersection of the habit planes predicted by the minimum incompatibility criterion. Position of the line is given by one fixed point preventing the microstructure from moving through the specimen as a whole.

Remaining parameters are the four angles (γ_1, γ_2, γ_3, γ_4) describing the orientations of two habit planes and two martensite–martensite interfaces (see Fig. 2.5). These angles represent deviations of respective planes from the reference planes, which are the planes closest to the corresponding minimum incompatibility planes and containing intersecting line given by **p**. The reference plane normals are obtained as a vector triple product $\mathbf{p}\times(\mathbf{p}\times\mathbf{n}_0)$, where $\mathbf{n}_0$ is a normal vector of the minimum incompatibility plane.

When the volume fractions are set to the values obtained from the classical theory and all six geometric parameters are set to zero, the habit planes are exactly the habit planes predicted by the classical theory and the martensite–martensite interfaces are the best approximations (in the sense of included angle) of the classical twinning planes, which intersect with the habit planes in one common line.

Since the objective function for the optimisation is in general nonconvex, the selection of the proper starting point is crucial. As mentioned above, it is supposed that the sought minimum lies close to the configuration predicted by the classical theory. Thus, as a starting point we set the volume fractions to values obtained from the classical theory and all geometric parameters are set to zero. As a optimisation algorithm the sequential quadratic programming algorithm with bounds is used. The bounds ensure that there is only one minimum within the searched range. When the optimal solution is found, we check that there are no active constraints.

2.3 Mobility of the Microstructure

In this section we try to construct a model describing the evolution of the observed microstructures, which should explain why such incompatible microstructures form.

Several classical approaches to model the martensitic phase transition are briefly discussed in [9], and [19]. They are mostly too general and none of them is able to deal with the particular microstructure. Latest published models involving microstructures ([12], [16]) do not try to predict which microstructure forms, but have a predefined type of the microstructure "imprinted" and describe the evolution of the parameters of this microstructure under various external conditions. This is also the way we follow.

To ensure relative simplicity of implementation we decided to base the model on suitable variational principle. The right choice strongly depends on the way how the dissipation mechanism is understood and described. In this aspect our model differs from the most of the others.

2.3.1 Spontaneous Isothermal Motion of non-Equilibrium Microstructures

In the quasistatic theory of evolution of martensitic microstructures under time dependent external loading (either thermal or mechanical), the dissipation is usually considered as strictly rate-independent, i.e. the dissipation rate is considered as 1-degree homogeneous in the time derivative of the volume fraction of the transformed phase (see [12] for more details and for an exhaustive list of relevant references). Such approach enables us to see a close analogy between the martensitic phase transition and plasticity, and to use the Hill's principle of maximal dissipation (principle of maximal plastic work [8]) to describe the evolution of the microstructure.

In [16] the problem of quasistatic loading and the related dissipation processes is discussed in more detail. The authors consider three different time scales coming into play. At the slowest scale, where the external loading is applied, the material moves through a sequence of quasi-stable states given by actual external conditions. The dissipation processes at this scale are strictly rate-independent and the evolution of the microstructure during some time increment Δt can be sufficiently described by the minimisation of the increment of the sum of the total Helmholtz free energy A and the dissipated energy D as follows:

$$\Delta E = \Delta A + \Delta D \rightarrow \min\,, \tag{2.25}$$

where the minimisation is done over all admissible changes of the microstructure.

However, there are two faster time scales, where the dissipation processes can be more general. At the fastest scale (processes at speeds comparable to propagation of elastic waves, namely the dynamic jumps of the lattice between the austenite and martensite or between the martensite variants) the main dissipative mechanism is the emission and consequent attenuation of acoustic waves (so called acoustic emission, see [15]). This contribution to the final dissipated energy can be considered as negligibly small (see the acoustic emission experiments in [19], documenting that the emission activity is maximal during the nucleation and annihilation of the interfacial microstructure, but that there are nearly no acoustic waves emitted during the stable propagation of the microstructure through the specimen).

On the contrary, a significant amount of energy is dissipated at the middle time scale, which is the scale capturing the spontaneous change of the microstructure due to a sudden change of external loadings. At this time scale, the loading parameters (temperature, applied stress) are kept constant defining a new equilibrium state towards which the system evolves. This is exactly the process we want to model (described in detail in [20]), where the specimen in martensite is put into a warm water bath (i.e. the temperature is suddenly increased and then kept approximately constant), which induces the formation and propagation of the microstructure in the material. The dissipative processes at this time scale (thermal effects, viscous dissipation) are, in principle, rate-dependent, although they appear as rate-independent at the slowest time scale.

Since there are no varying external conditions in our case, “nothing happens” at the slowest time scale, so we must describe the modelled process at the faster one. This implies that the considered dissipation must be rate-dependent. Then the speed of the microstructure evolution is controlled by the dissipation rate.

We can consider that the energy dissipated during such process is equivalent to the work done by dissipative (or friction-like) forces, and formulate a variational condition analogous to (2.25) in rates

$$\dot{E} = \dot{A} + \frac{1}{2}\int_{\mathcal{V}} \sigma_{ij}^{\mathrm{d}iss.}\dot{\epsilon}_{ij}\,\mathrm{d}\mathbf{x} \to \min\,, \tag{2.26}$$

where $\sigma_{ij}^{\mathrm{d}iss.}$ is a *dissipative stress tensor* and the finite strain tensor ϵ is defined as

$$\epsilon = \frac{1}{2}(\nabla\widetilde{\mathbf{y}}^{\mathrm{T}}\nabla\widetilde{\mathbf{y}} - \mathbf{I})\,. \tag{2.27}$$

Thus, it involves the inelastic transformation strains as well as the elastic strains.

The minimum is sought not only with respect to all admissible spatial evolutions $\epsilon_{ij}(t)$ of the microstructure but also with respect to the velocities $\dot{\epsilon}_{ij}(t)$. In fact, the extremal condition (2.26) can be understood as a particular form of the Biot's principle (see [8]) for rate-dependent dissipative systems.

2.3.2 Mobility Modelling of the Lambda and X Microstructures

To describe the state of the microstructure the parametrisation introduced in 2.2.2 is used providing two extra parameters $\mathbf{X} = [x_h, x_v]$ defining the intersecting line position. These parameters stand for the coordinates of the crossing point in the face A in the local coordinate system attached with the lower left corner of the face. Hence, all properties of the microstructure depend on the ten parameters (x_h, x_v, λ_1, λ_2, θ, ϕ, γ_1, γ_2, γ_3, γ_4).

The dissipative tensor $\sigma_{ij}^{\text{diss.}}$ can be considered in a general form

$$\sigma_{ij}^{\text{diss.}} = \eta_{ijkl}\dot{\epsilon}_{kl} \, , \tag{2.28}$$

where η_{ijkl} is a *viscosity tensor*, see [14]. Since there are no experimental data for constants η_{ijkl}, the simple isotropic form is used. For an isotropic body this tensor has only two independent components, so the dissipative tensor can be written in the form

$$\sigma^{\text{diss.}} = \mu_V \frac{\operatorname{tr}\dot{\epsilon}}{3}\mathbf{I} + \mu_S\left(\dot{\epsilon} - \frac{\operatorname{tr}\dot{\epsilon}}{3}\mathbf{I}\right) \, , \tag{2.29}$$

where the *bulk viscosity* μ_V is related mostly to the thermoelasticity and the *shear viscosity* μ_S is related to the viscous motion of dislocations and twin boundaries.

For simplicity, we will consider the values of μ_V and μ_S to be the same both inside all individual phases (martensite, twinned martensite, austenite) and at the interfaces. Thus, the finite jumps in ϵ_{ij} at the interface planes ensure that most of the energy is dissipated by the moving interfaces.

The temperature is fixed above the transformation temperature. Thus, the total free energy A is assumed in the form (2.17), where for the elastic part W_e the relation (2.18) holds and where the transformation part W is assumed to be a linear function of the martensite and austenite volumes $\mathcal{V}_m$ and $\mathcal{V}_a$:

$$A = W + E_e = c_m\mathcal{V}_m + c_a\mathcal{V}_a + E_e \, . \tag{2.30}$$

Putting previous equations together we obtain (keep in mind that all properties are functions of the microstructure parameters defined above)

$$\begin{aligned}\dot{E} = \dot{A} + \dot{D} = c_m\dot{\mathcal{V}}_m + c_a\dot{\mathcal{V}}_a + \dot{E}_e + \frac{1}{2}\int_{\mathcal{V}}\left(\mu_V\frac{\dot{\epsilon}_{kk}}{3}\delta_{ij} + \mu_S\left(\dot{\epsilon}_{ij} - \frac{\dot{\epsilon}_{kk}}{3}\delta ij\right)\right)\dot{\epsilon}_{ij}\,\mathrm{d}\mathbf{x} = \\ = c_m\dot{\mathcal{V}}_m + c_a\dot{\mathcal{V}}_a + \dot{E}_e + \frac{1}{2}\int_{\mathcal{V}}\frac{\mu_V - \mu_S}{3}\left(\operatorname{tr}\dot{\epsilon}\right)^2 + \mu_S\operatorname{tr}\left(\dot{\epsilon}^2\right)\,\mathrm{d}\mathbf{x} \to \min \, .\end{aligned} \tag{2.31}$$

The constants c_m, c_a, μ_V, and μ_S remaining to be supplied are discussed later in 3.3.1. The objective is to find the set of the functions ($x_h(t)$, $x_v(t)$, $\lambda_1(t)$, $\lambda_2(t)$, $\theta(t)$, $\phi(t)$, $\gamma_1(t)$, $\gamma_2(t)$, $\gamma_3(t)$, $\gamma_4(t)$), which minimises $\dot{E}$ (or in the other words, maximises the energy release rate). We are particularly interested in the first two parameters describing the motion of the whole microstructure.

Discretisation and Solution

To solve the problem (2.31) the time is discretised and the time derivatives are replaced by finite differences:

$$\begin{aligned}\dot{E} \approx \frac{A_{n+1} - A_n}{\Delta t_{n+1}} + &\\ + \frac{1}{2} \int_{\mathcal{V}} \frac{\mu_V - \mu_S}{3} \left(\operatorname{tr} \frac{\epsilon_{n+1} - \epsilon_n}{\Delta t_{n+1}} \right)^2 + \mu_S \operatorname{tr} \left(\left(\frac{\epsilon_{n+1} - \epsilon_n}{\Delta t_{n+1}} \right)^2 \right) \mathrm{d}\mathbf{x} = &\\ = (A_{n+1} - A_n) \frac{1}{\Delta t_{n+1}} + &\\ + \frac{1}{2(\Delta t_{n+1})^2} \int_{\mathcal{V}} \frac{\mu_V - \mu_S}{3} \left(\operatorname{tr} \left(\epsilon_{n+1} - \epsilon_n \right) \right)^2 + \mu_S \operatorname{tr} \left(\left(\epsilon_{n+1} - \epsilon_n \right)^2 \right) \mathrm{d}\mathbf{x} \to \min \, , \quad (2.32)\end{aligned}$$

where

$$\begin{aligned} A_n &= A\big(x_h(t_n), x_v(t_n), \lambda_1(t_n), \lambda_2(t_n), \theta(t_n), \phi(t_n), \gamma_1(t_n), \gamma_2(t_n), \gamma_3(t_n), \gamma_4(t_n)\big) \, , \\ \epsilon_n &= \epsilon\big(x_h(t_n), x_v(t_n), \lambda_1(t_n), \lambda_2(t_n), \theta(t_n), \phi(t_n), \gamma_1(t_n), \gamma_2(t_n), \gamma_3(t_n), \gamma_4(t_n)\big) \, , \\ \Delta t_{n+1} &= t_{n+1} - t_n \, . \end{aligned} \tag{2.33}$$

With the given time step and two sets of microstructure parameters the equation (2.32) approximates the value of $\dot{E}$ along the path from the first given state to the second one. Thus, for the given state of the microstructure in the time t_n and fixed time step, we can find the state at the time t_{n+1} by minimisation of $\dot{E}$ with respect to the new microstructure parameters. Reiterating this procedure we get the time evolution of the microstructure. Every step comprises optimisation with respect to ten parameters. With the a little trick the dimension of the problem can be shrank by one.

Providing

$$\begin{aligned} \Delta A_{n+1} &= A_{n+1} - A_n \, , \\ \widetilde{D}_{n+1} &= \frac{1}{2} \int_{\mathcal{V}} \frac{\mu_V - \mu_S}{3} \left(\operatorname{tr} \left(\epsilon_{n+1} - \epsilon_n \right) \right)^2 + \mu_S \operatorname{tr} \left(\left(\epsilon_{n+1} - \epsilon_n \right)^2 \right) \mathrm{d}\mathbf{x} \end{aligned} \tag{2.34}$$

the equation (2.32) can be written in the form

$$\dot{E} \approx \Delta A_{n+1} \frac{1}{\Delta t_{n+1}} + \widetilde{D} \frac{1}{(\Delta t_{n+1})^2} \, . \tag{2.35}$$

Notice that (2.35) is a quadratic function in the variable $\frac{1}{\Delta t_{n+1}}$ with coefficients ΔA_{n+1} and $\widetilde{D}$, which depends only on the microstructure parameters. If we are able to express any of the sought parameters in the terms of Δt_{n+1}, then the optimisation with respect to this parameter can be replaced by the optimisation with respect to Δt_{n+1}. The formula for the optimal value of Δt_{n+1} is obvious and can be easily derived from the equation (2.35).

Let us rewrite the parameters describing the crossing point position at the time t_{n+1} in the following way:

$$\begin{aligned} x_{h,n+1} &= x_{h,n} + v_{n+1}\Delta t_{n+1}\cos(\eta_{n+1}) = \Delta x_{n+1}\cos(\eta_{n+1}) \\ x_{v,n+1} &= x_{v,n} + v_{n+1}\Delta t_{n+1}\sin(\eta_{n+1}) = \Delta x_{n+1}\sin(\eta_{n+1})\,. \end{aligned} \tag{2.36}$$

The sought parameters $x_{h,n+1}$ and $x_{v,n+1}$ were replaced by the v_{n+1}, which has a meaning of scalar velocity of the crossing point, and η_{n+1}, which is an angle describing the direction of movement of the crossing point. The $\Delta x_{n+1} = v_{n+1}\Delta t_{n+1}$ denotes the spatial step length. With the fixed time step the velocity is given by the spatial step length, but for the fixed $\Delta x_{n+1} = \Delta x$, the velocity is fully determined by the time step Δt_{n+1}. Hence, with the fixed spatial step length the optimisation with respect to parameter $x_{h,n+1}$ and $x_{v,n+1}$ can be replaced with the optimisation with respect to angle η_{n+1} and the time step Δt_{n+1}.

The optimal value of the time step is found as an argument of the minimum of the quadratic function (2.35):

$$\Delta t_{n+1} = -\frac{2\widetilde{D}_{n+1}}{\Delta A_{n+1}}\,. \tag{2.37}$$

Eliminating Δt_{n+1} from (2.35) yields

$$\dot{E} \approx -\frac{(\Delta A_{n+1})^2}{4\widetilde{D}_{n+1}}\,. \tag{2.38}$$

Recall that provided fixed step length Δx the quantities ΔA_{n+1} and $\widetilde{D}_{n+1}$ depend on the initial state, on the direction η_{n+1}, and on the remaining eight parameters. Thus, the optimisation has to be done with respect to nine parameters now. We employ the same SQP algorithm as in the previous section.

Substituting (2.37) to (2.35) an interesting relation can be obtained:

$$\frac{\Delta A_{n+1}}{\Delta t_{n+1}} + 2\frac{\Delta D_{n+1}}{\Delta t_{n+1}} = 0\,. \tag{2.39}$$

It means that for the optimal choice of time step length (i.e. the velocity of the motion) the dissipation rate is a minus half of the free energy change rate. And thus, the total energy change rate is a half of the free energy change rate:

$$\dot{E} \approx \frac{1}{2}\frac{\Delta A_{n+1}}{\Delta t_{n+1}}\,. \tag{2.40}$$

Notice that the term on the right hand side of the equation (2.38) is always non-negative. It looks like that total energy E never increases for any virtual change of the microstructure (constrained to the fixed step length Δx), but it is not true. The admissibility of particular virtual change is governed by the equation (2.37). If the total free energy A increases or remains constant with the given virtual change, the optimal time step length becomes negative or “infinite”, which is meaningless. Hence, the motion is possible if and only if the total free energy decreases. Therefore, for the purpose of optimisation we use the $\mathrm{sgn}(\Delta t_{n+1})\dot{E}$ as the objective function.

Chapter 3

Implementation and Results

This chapter presents numerical results for introduced models and describes some implementation details. All computations were done in MATLAB environment in connection with COMSOL Multiphysics FEM software package, which provides a bidirectional scripting interface to MATLAB.

3.1 Elastic Strain Evaluation

The evaluation of the elastic strain field and stored elastic energy for the given geometry of the microstructures forms an integral part of all computations. The problem defined in 2.2.1 is solved by the finite element method. Only one additional boundary condition is set. Since the solution of the problem is unique up to arbitrary rotation, we fix the base of the specimen.

3.1.1 Model Implementation in COMSOL Multiphysics

The implementation in COMSOL Multiphysics (see [1] for documentation) is quite straightforward. We use *Solid, Stress-Strain* application mode defined in *Structural Mechanics module* with most of settings set to default. This mode is intended to solve 3D solid deformation problems. The used variational formulation is based on the principle of virtual work.

The initial geometry determined by the microstructure parameters is generated by set of MATLAB scripts. As a result the separate four geometric objects are obtained, which represent different parts of the microstructure after the inelastic deformation according to the macroscopic deformation gradients (see 2.2.1).

The COMSOL Multiphysics *Use Assembly* option enables us to work with separate volumes and to generate an independent mesh for each one. This allows displacement field to be discontinuous over the interfaces. The coupling boundary conditions (2.24) are set through the *Extrusion Coupling Variables* option.

Since we are working in the regime of small deformations (i.e. linear elasticity), the system of equations obtained by the FEM discretisation is linear. To solve the system we use a provided PARDISO direct solver implementing LU decomposition with nested dissections preordering suitable for parallel computation.

3.1.2 Mesh Settings, Convergence

Since all parts of our geometry are of the similar length-scale, there is no need for any extra fine mesh. On the boundaries, where the "glueing" condition is prescribed, it is required that the affine transform, which maps these boundaries one to another, maps also the corresponding boundary meshes one to another. Otherwise, the pointwise conditions (2.24) give arise to some numerical artifacts. This requirement is fulfilled by use of *mapped mesh* function. The mapped mesh is created according to profile *finer* and converted to triangular mesh. The rest of the geometry is meshed with tetrahedral elements according to profile *fine*.

The resulting mesh comprises approximately 5,000 elements. Since the Lagrange cubic finite elements are used, the obtained mesh has about 80,000 degrees of freedom.

When the mesh was refined by decreasing the element size by the factor of two, the stored elastic decreased by less then 0.25%. At the same time it was checked that the accuracy is sufficient to catch a feasible geometric parameters change. Thus, these settings are used in all the following computations.

3.2 Modelling of the Stable Microstructures

The proposed modified model of stable martensitic microstructures 2.2 was used to model observed lambda and X microstructure. The optimal geometry was computed for the crossing point positions taken from the experiments.

3.2.1 Optimisation Settings, Convergence

The stored elastic energy was minimised with respect to volume fractions and geometric parameters introduced in 2.2.2. We used the MATLAB Optimization Toolbox function *fmincon()*, which solves the problem by sequential quadratic programming algorithm with BFGS hessian update.

angle $\setminus$ *face*	**A**	**B**	**C**
$\Delta(\mathbf{m}_{AB}, \mathbf{m}_X)$	0.6°		0.3°
$\Delta(\mathbf{m}_{AB}, \mathbf{m}_{CD})$	-2.6°		-3.6°
$\Delta(\mathbf{n}_{AB}, \mathbf{m}_{CD})$	-2.2°		-0.3°
$\Delta(\mathbf{n}_{AB}, \mathbf{m}_X)$	-0.9°		-1.9°
$\Delta(\mathbf{m}_{AB}, \mathbf{n}_{AB})$	-1.5°		-2.8°
$\Delta(\mathbf{m}_{CD}, \mathbf{m}_X)$	-2.4°	0.5°	-2.1°
$\Delta(\mathbf{m}_{AB}, \text{edge})$	1.0°		1.3°
$\Delta(\mathbf{n}_{AB}, \text{edge})$	-0.1°		-0.2°
$\Delta(\mathbf{m}_{CD}, \text{edge})$	3.5°	1.0°	1.4°
$\Delta(\mathbf{m}_X, \text{edge})$	1.2°	1.6°	0.6°

Table 3.1: Differences between the computed and measured angles for the lambda microstructure

The optimal geometric parameters were sought within the interval $(-2^\circ, 2^\circ)$, for the volume fractions we set the lower bound to 0.25 and upper bound to 0.35. Initial values were zeroes for the geometric parameters and 0.3008 for the both volume fractions (this value is provided by the classical theory).

The minimal step length for the finite differentiation was set to 0.01. Since the objective function is very sensitive to volume fractions parameters, these were rescaled by the scaling factor 100. Objective function value tolerance for the stopping criterium was set to 0.0005 mJ, which is approximately 0.01% of the optimal value.

In all cases the optimisation stopped within 14 iterations, when projected objective function change was less than given tolerance. Found point was checked for optimality also manually by evaluating all forward and backward finite differences in that point with step length 0.005.

3.2.2 Results

For the observed lambda microstructure the optimal volume fractions found are 0.2955 for the {**A**:**B**} twinning system and 0.2977 for the {**C**:**D**} twinning system. These values are slightly less than the values predicted by the classical theory. The optimal geometric parameters are $\vartheta = 0.36^\circ$, $\phi = 0.22^\circ$, and gammas $(0.08^\circ, -0.12^\circ, -0.32^\circ, 0.38^\circ)$. The deviations are small, so the configuration predicted by the classical theory lies very close to the energetical optimum. Differences between the optimal and observed angles are summarised in Tab. 3.1. Since the twinned regions are treated as homogeneous, the orientation of the twinning plane in the {**C**:**D**} twinning system cannot be predicted. See Fig. A.3 for graphical representation of the results, where the original optical micrographs are overlaid by the computed geometry. In the Fig. A.5

angle ∖ *face*	**A**	**B**	**C**	**D**
$\Delta(\mathbf{m}_{AB}, \mathbf{n}_{CB})$	$3.0°$		$3.0°$	
$\Delta(\mathbf{m}_{AB}, \mathbf{m}_{CB})$	$-4.0°$		$-3.4°$	
$\Delta(\mathbf{n}_{AB}, \mathbf{n}_{CB})$	$1.2°$		$1.2°$	
$\Delta(\mathbf{n}_{AB}, \mathbf{m}_{CB})$	$2.3°$		$1.3°$	
$\Delta(\mathbf{m}_{AB}, \mathbf{n}_{AB})$	$-1.8°$		$-1.7°$	$-1.1°$
$\Delta(\mathbf{m}_{CB}, \mathbf{n}_{CB})$	$-1.0°$	$0.3°$	$-0.1°$	
$\Delta(\mathbf{m}_{AB}, \text{edge})$	$1.2°$		$1.2°$	$-1.4°$
$\Delta(\mathbf{n}_{AB}, \text{edge})$	$0.4°$		$1.1°$	$-0.6°$
$\Delta(\mathbf{m}_{CB}, \text{edge})$	$2.4°$	$0.1°$	$2.9°$	
$\Delta(\mathbf{n}_{CB}, \text{edge})$	$-1.8°$	$0.3°$	$-1.8°$	

Table 3.2: Differences between the computed and measured angles for the X microstructure

and Fig. A.6 the volume stress (one third of the hydrostatic stress tensor trace) and the Tresca stress (represents shear stress) are plotted.

Situation for the X microstructure is similar. The found volume fractions are 0.2956 and 0.2947, $\vartheta = -0.81°$, $\phi = 0.35°$, and gammas ($-0.10°$, $-0.25°$, $-0.60°$, $1.09°$). Again, the optimal configuration lies close to that predicted by the classical theory. Differences between optimal and observed angles are summarised in Tab. 3.2. The overlay of computed geometry and observed geometry can be seen in Fig. A.4. In the Fig. A.7 and Fig. A.8 the volume stress and the Tresca stress are plotted. Notice that in the case of the X microstructure the stresses are significantly higher than in the lambda microstructure. But this was expected, since Fig. 2.3 shows that the geometric misfit in the X microstructure is noticeably larger.

Comparing table Tab. 2.3 with Tab. 3.1 and Tab. 2.5 with Tab. 3.2 we can see that the predictions obtained from our model are not much better than predictions of the classical theory. In fact, the mean differencies are somewhat higher. It is supposed that this issue is related to many simplifications done in the model. Particularly, the twinned regions were homogenised, and all interfaces are assumed to be exact planes, which may not be true.

3.3 Modelling of the Microstructure Mobility

Here we present results based on the model of microstructure mobility introduced in 2.3. First, we examine mobility of the both lambda and X microstructures in five different configurations by evaluating the energy release rate and velocity for the various crossing point moving directions. Next, some results of optimisation procedure proposed in 2.3.2

parameter	*value*
c_a	0 J.m^{-3}
c_m	5×10^7 J.m^{-3}
μ_V	3.36×10^{10} Pa.s
μ_S	1.2×10^9 Pa.s

Table 3.3: Model parameters

describing microstructure evolution are presented.

3.3.1 Model Parameters

The model depends on four yet unspecified constants—the transformation parts of the free energy density of the martensite and austenite (c_m, c_a), and two viscosity constants (bulk viscosity μ_V, shear viscosity μ_S). Unfortunately, there are no (or poor) experimental estimates of these constants. Thus, we choose them so that the model fits observations in the main properties.

The energy densities c_m and c_a are defined up to an additive constant and the model depends on their difference only, thus we set $c_a = 0$ J.m^{-3}. The shear viscosity μ_S related to motion of dislocations is chosen to be approximately ten times smaller than the bulk viscosity. The absolute values of the constants were fitted to observed crossing point movement velocity and expected latent heat absorption rate, which was supposed to be higher but comparable to the dissipation rate (according to infrared microscopy observations in [19] the specimen is undercooled by the microstructure motion). Here, the velocity (about 2 mm.s^{-1}) was taken from [19] and the laten heat of the transition was taken from [2]. See Tab. 3.3 for obtained parameters.

Notice that the time derivative of the first term of (2.30)

$$\dot{W} = c_m \dot{\mathcal{V}}_m + c_a \dot{\mathcal{V}}_a \tag{3.1}$$

is 1-degree homogeneous in transformed volume change rate, since $\dot{\mathcal{V}}_m = -\dot{\mathcal{V}}_a$. Thus, in fact, it represents not only the change of the transformation part of the free energy, but it can also comprise the rate-dependent part of the dissipation.

3.3.2 Microstructure Mobility Investigation

To get an idea of the nature of the total energy change rate and crossing point velocity ($v = \frac{\Delta x}{\Delta t}$) dependence on the motion direction we evaluated these quantities according to (2.38) and (2.37) for one step in all admissible directions from the given starting

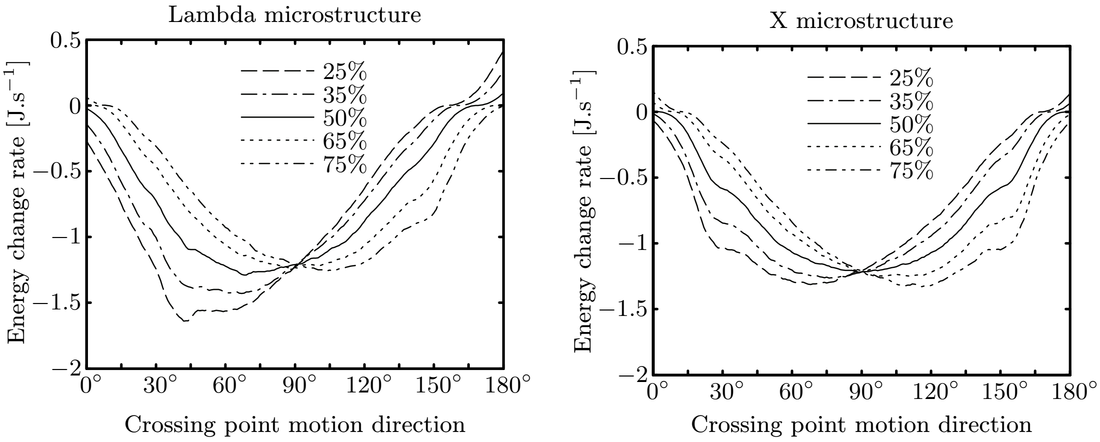

Figure 3.1: Total energy change rate profile for various starting configurations

configurations. In addition, also the total energy decrement values $\Delta E = \dot{E}\Delta t$ were computed (according to (2.40) it is equal to a half of the free energy decrement).

To obtain starting configuration of the microstructure we ran the optimisation procedure from 2.2.2 for the chosen crossing point position. We chose five distinct crossing point positions in the same distance from the bottom (shorter) edge of the face A (the distance was set to 35% of the face length), but with different distances from the left edge of the face A. The distances are 25%, 35%, 50%, 65%, and 75% of the face width (so the 0% means the position exactly at the left edge and 100% stands for the position at the right edge of the face A).

The spatial step length Δx was set to 10% of the face A width, other microstructure parameters were fixed. The observed quantities were evaluated for spatial step direction η running from 0° to 180° with 1° step. Here, the 0° means motion towards the right edge of the face and 90° means motion parallel with the longer edges towards the martensite region. In other directions the volume of the austenite always decreases, which nearly always leads to free energy increase and thus to inadmissible motion.

Results

The plots of the all results for the both microstructures under investigation can be seen in Fig. 3.1, Fig. 3.2, and Fig. 3.3. Since the computed data were little noisy, they were smoothed by moving average method with 3° window size.

Although the configurations are not symmetric, all lines intersect at 90° direction. This is because of with this direction the amount of transformed and reoriented material is the same regardless of the crossing point position. The changes of the stored elastic energy and the elastic strains are incomparably smaller than the changes of the total

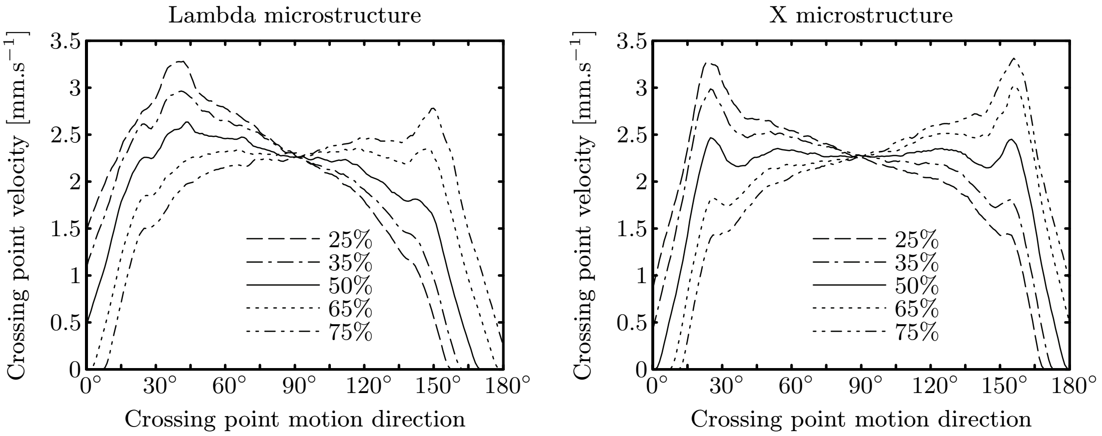

Figure 3.2: Crossing point velocity profile for various starting configurations

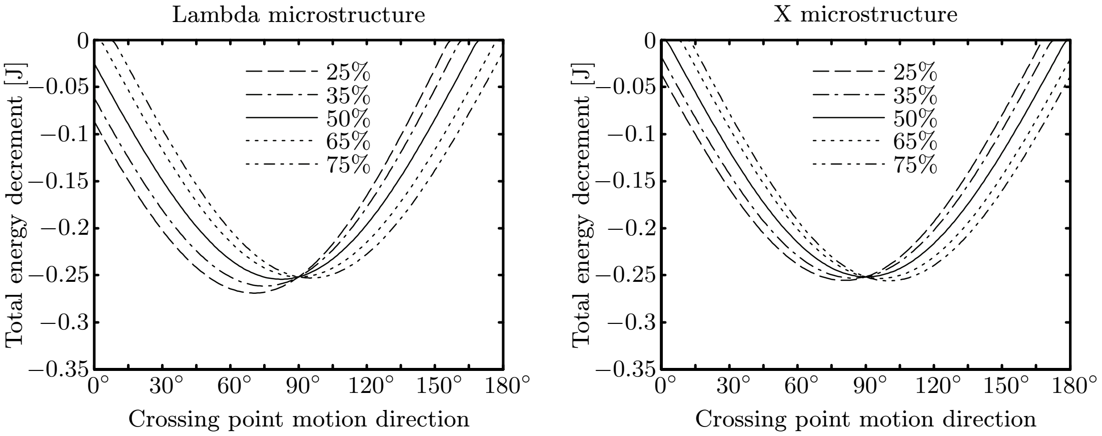

Figure 3.3: Total energy decrement profile for various starting configurations

free energy and the inelastic transformation strains, thus the elasticity has a negligible influence on the microstructure motion direction and speed . Hence, the change of the free energy as well as the dissipation (and thus velocity) remains same for all crossing point positions.

Another visualisation of the results is shown in Fig. 3.4 and Fig. 3.5, where the absolute values of the quantities are plotted for the each crossing point position in polar coordinates with the highest values marked (the quantities were rescaled and shifted to fit in one plot). The smaller half circle (full line) denotes the zero value.

It is clearly visible here that the optimal direction (represented by the total energy release rate maximum) is a result of "competition" between the direction of maximal free energy decrease, which varies continuously with the crossing point position, and the direction of minimal dissipation (i.e. maximal velocity), which changes abruptly, when

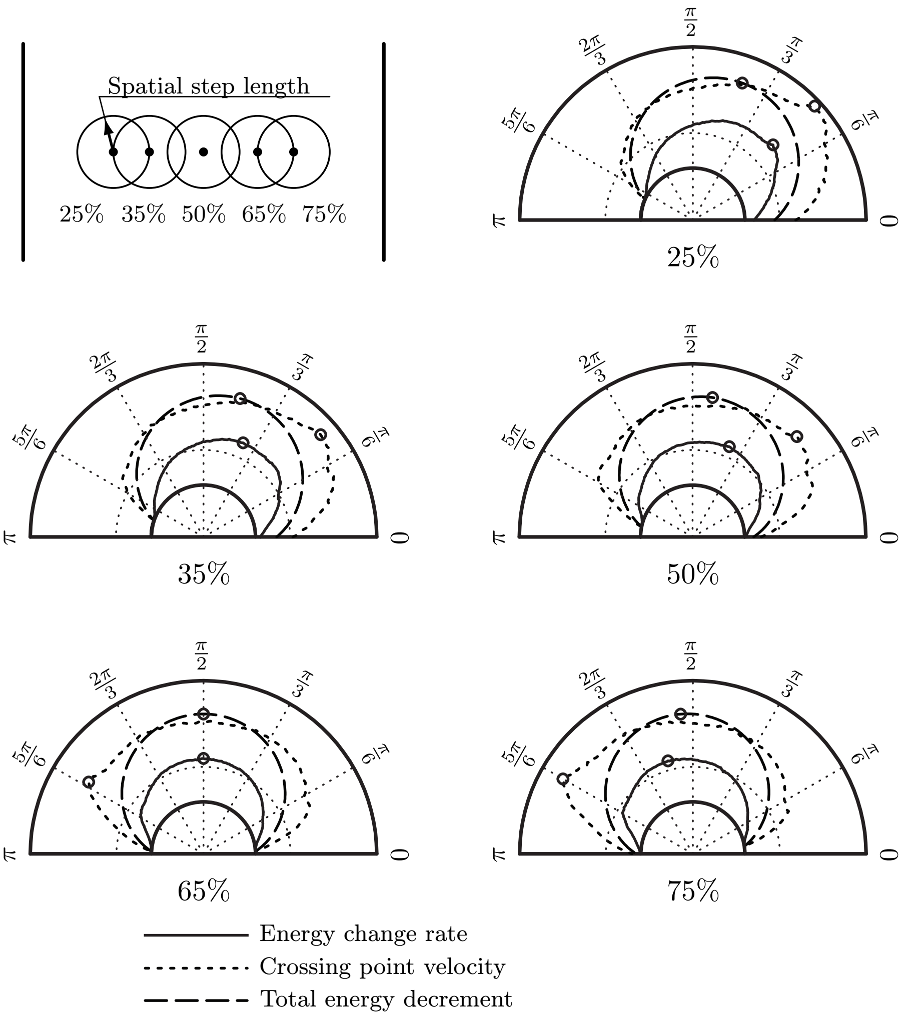

Figure 3.4: Lambda microstructure mobility visualisation

the crossing point passes the middle position. Notice that the locations of the velocity local maxima are constant for the given microstructure (clearly visible in Fig. 3.2). The maximum velocity directions correspond to a crossing point motions along the martensite–twinned martensite interface, since during this motion dissipation occurs at two interfaces only, other two interfaces do not move.

But the most important observation is that according to our model the crossing point tends to move away from the edges even though it means to form incompatible microstructure with higher stored elastic energy.

3.3.3 Microstructure Evolution

The evolution of the all microstructure parameters is governed by the model from 2.3.2. It comprises a ten-parametric optimisation of the total energy release rate objective

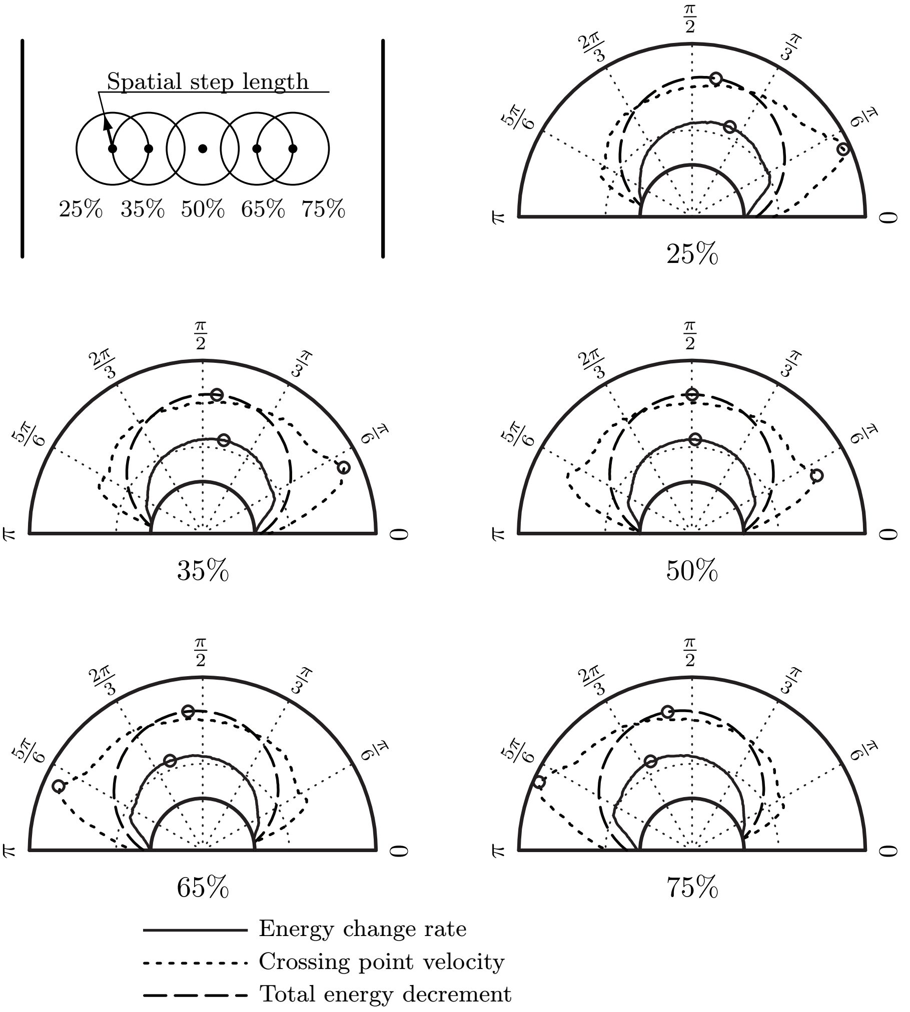

Figure 3.5: X microstructure mobility visualisation

function at the each step.

The procedure is similar to that from the 3.3.2. For the chosen crossing point starting position the optimal configuration of the stable microstructure was found and this configuration was used as a starting configuration in the sequence describing the evolution. Following members of the sequence were obtained by optimisation of the objective function (2.38).

For the both microstructures the 10 successive configurations were computed with two distinct starting points. The first starting configuration corresponds to the crossing point positioned near the right edge of the face A (20%), the second corresponds to the position near the left edge (80%). Distance from the bottom edge was the same as in the previous section (35% of the face length).

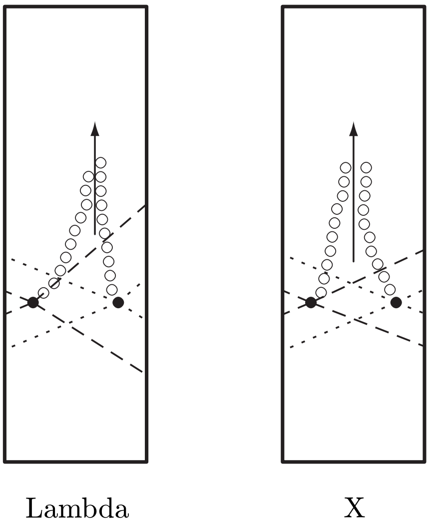

Figure 3.6: Predicted crossing point paths during the microstructure evolution from the two different starting configurations

Optimisation Settings, Convergence

The spatial step length was again set to 10% of the face A width. The initial point for the each optimisation was defined by the previous configuration, where as the starting direction η_0 the 90° was taken. Since the volume fractions are not supposed to change during the motion, we omit them in the optimisation, and thus optimise with respect to eight parameters only. The directions η_n were sought through the full range from -180° to 180° , except the λ_1 the lower and upper bounds for the other parameters was set to -4 and 4 respectively. In the case of the lambda microstructure and initial crossing point position near the right edge the upper bound for the λ_1 parameter had to be raised to 8. Finite differentiation settings and function value tolerance remain same as in 3.2.1, but now the value of 0.0005 J.s^{-1} equals to 2–3% of the objective function optimal value. Also, the objective function was rescaled in the direction parameter with a factor $\frac{1}{100}$, so that the minimal step for the finite difference evaluation is 3° .

Mostly the optimisation algorithm stopped within 5 iterations, but in some cases it took up to 9 iterations, till the projected objective function change was less than the given tolerance. Further optimality tests were not done.

Results

The projected paths in the face A of the crossing point position for the both microstructures and both starting configurations are shown in Fig. 3.6. As we can see, from the both sides the crossing point moves forward and simultaneously away from the edge

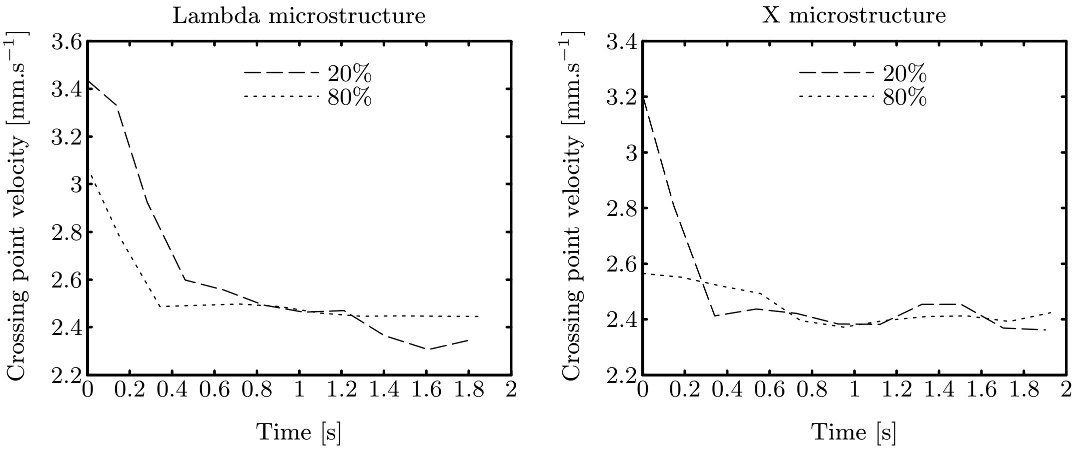

Figure 3.7: Crossing point velocity during the microstructure evolution from the two different starting configurations

(i.e. the microstructure grows). Finally, the paths meet and continue almost in one line parallel to the side edges. For the X microstructure this line passes through the centre of the face, whereas in the case of the lambda microstructure the line distance form the left edge is about 65% of the bottom edge length. This expectable behavior follows also from Fig. 3.5 and Fig. 3.4.

The computed velocity of the crossing point is illustrated in Fig. 3.7. The behavior of the velocity is in agreement with experimental observations reported in [19]. Within these observations the velocity drops, when the microstructure is fully formed and further remains almost constant. This is because of low dissipation during the microstructure formation, when only two interfaces are moving.

Unfortunately, the optimisation did not provide desirable results for the other microstructure parameters. Obtained orientations of the interfaces evolve discontinuously and differ to much from the observed ones (sometimes the difference is higher than 5°). The first problem is caused by deficient accuracy of the objective function response to the direction parameter, which breaks the line-search phase of the optimisation. We impute the second issue to possibly different time scales, at which the whole microstructure motion (slow) and the elastic strains relaxation (fast) take place as proposed in [16]. Thus, these two processes should not be mixed together in one optimisation procedure.

We believe that both problems can be solved by replacing the current "big" optimisation with two nested optimisation procedures. The inner one minimises the stored elastic energy with respect to orientations of the interfaces for the given microstructure position as in 2.2.2. Then, the outer one finds the optimal direction of motion according to maximal energy release rate principle as described in 2.3. For the outer optimisation some derivative free algorithm can be chosen (e.g. some of the response surface algorithms).

Conclusions

We proved that the briefly introduced mathematical theory of martensites developed by Ball and James ([4]) does not allow us to handle observed lambda and X microstructures, since they are not global minimisers of the free energy. It was shown that requiring only a local optimality we are able to describe these incompatible microstructures and predict their parameters in a good agreement with the experiments.

We constructed a model governing the spontaneous evolution of the microstructure under the constant external conditions. The main difference from the most of the other published models is in incorporation of the rate-dependent dissipation mechanism, which enables us to describe fast evolution processes.

Due to the lack of the experimental data the model parameters had to be fitted to observations. Therefore, the comparison of the model predictions with the experiments is meaningless. However, we showed that our model is able to catch the main properties of the microstructure evolution.

The model can be further improved by an implicit integration of additional physical processes, especially the thermal effects. We believe that by supplying more information from the shorter length scales we can also significantly extend the model validity range.

Bibliography

[1] C. AB. *COMSOL Multiphysics Modeling Guide* (version 3.5a). [cited at page(s) 47]

[2] R. Abeyaratne and J. K. Knowles. On the kinetics of an austenite → martensite phase transformation induced by impact in a Cu–Al–Ni shape-memory alloy. *Acta Materialia*, 45(4):1671–1683, 1997. [cited at page(s) 51]

[3] X. Balandraud and G. Zanzotto. Stressed microstructures in thermally induced M9R-M18R martensites. *Journal of the Mechanics and Physics of Solids*, 55(1):194–224, January 2007. [cited at page(s) 38]

[4] J. M. Ball. Mathematical models of martensitic microstructure. *Material Science and Engineering*, 2003. [cited at page(s) 1, 3, 17, 59]

[5] Z. Basinski and J. Christian. Experiments on the martensitic transformation in single crystals of indium–thallium alloys. *Acta Metallurgica*, 2(1):148–166, 1954. [cited at page(s) 25]

[6] K. Bhattacharya. *Microstructure of Martensite.* Oxford University Press, New York, 2003. [cited at page(s) 4, 6, 8, 9, 11, 12, 13, 14, 15, 18, 19, 21, 71]

[7] K. Bhattacharya, S. Conti, G. Zanzotto, and J. Zimmer. Crystal symmetry and reversibility of martensitic transformations. *Nature*, 428(6978):55–59, 2004. [cited at page(s) 11]

[8] Y.-C. Fung. *Foundations of Solid Mechanics.* Prentice-Hall, 1965. [cited at page(s) 40, 42]

[9] O. Glatz. Matematické modelování fázových transformací v monokrystalech slitin s tvarovou pamětí. Bachelor thesis, Czech Technical University in Prague, Prague, 2008. [cited at page(s) 3, 40]

[10] K. F. Hane. *Microstructures in Thermoelastic Martensites.* PhD thesis, University of Minnesota, 1998. [cited at page(s) 12, 14, 21, 23]

[11] R. D. James and Z. Zhang. A way to search for multiferroic materials with "unlikely" combinations of physical properties. In *Magnetism and Structure in Functional Materials*, number 79 in Springer Series in Materials Science, chapter 9, pages 159–174. Springer, 2005. [cited at page(s) 18]

[12] M. Kružík, A. Mielke, and T. Roubíček. Modelling of microstructure and its evolution in shape-memory-alloy single-crystals, in particular in CuAlNi. *Meccanica*, 40(4–6):389–418, 2005. [cited at page(s) 40]

[13] M. Landa, P. Sedlák, H. Seiner, L. Heller, L. Bicanová, P. Šittner, and V. Novák. Modal resonant ultrasound spectroscopy for ferroelastics. *Applied Physics A: Materials Science & Processing*, 96(3):557–567, 2009. [cited at page(s) 37]

[14] L. D. Landau and E. M. Lifshitz. *Theory of Elasticity*, volume 7 of *Course of Theoretical Physics*. Butterworth–Heinemann, 3 edition, 1986. [cited at page(s) 36, 42]

[15] V. Novák, M. Landa, and P. Sittner. Acoustic recognition of stress induced martensitic transformations in Cu-based shape memory alloys. *Journal de Physique IV*, 112(1):593–596, 2003. [cited at page(s) 41]

[16] H. Petryk and S. Stupkiewicz. Interfacial energy and dissipation in martensitic phase transformations. Part I: Theory. *Journal of the Mechanics and Physics of Solids*, 2009. [cited at page(s) 1, 40, 57]

[17] G. Ruddock. A microstructure of martensite which is not a minimiser of energy: the X-interface. *Archive for Rational Mechanics and Analysis*, 127(1):1–39, September 1994. [cited at page(s) 35]

[18] P. Sedlák, H. Seiner, M. Landa, V. Novák, P. Šittner, and L. Mañosa. Elastic constants of bcc austenite and 2H orthorhombic martensite in CuAlNi shape memory alloy. *Acta Materialia*, 53(13):3643–3661, August 2005. [cited at page(s) 22]

[19] H. Seiner. *Dynamic and Transient Phenomena in Single Crystals of Shape Memory Alloys*. PhD thesis, Czech Technical University in Prague. Faculty of Nuclear Sciences and Physical Engineering, 2008. [cited at page(s) 1, 40, 41, 51, 57]

[20] H. Seiner, M. Landa, and P. Sedlák. Shape recovery mechanism observed in single crystals of Cu–Al–Ni shape memory alloy. *Phase Transitions*, 81(6):537–551, June 2008. [cited at page(s) 25, 41]

[21] S. Stupkiewicz, G. Maciejewski, and H. Petryk. Low-energy morphology of the interface layer between austenite and twinned martensite. *Acta Materialia*, 55(18):6292–6306, August 2007. [cited at page(s) 29]

[22] V. Valvoda, M. Polcarová, and P. Lukáč. *Základy strukturní analýzy*. Karolinum, Prague, 1 edition, 1992. [cited at page(s) 9]

[23] S. Vedantam and R. Abeyaratne. A helmholtz free-energy function for a Cu-Al-Ni shape memory alloy. *International Journal of Non-Linear Mechanics*, 2005. [cited at page(s) 10, 71]

[24] T. Will. *Singular Value Decomposition* [online]. c1999, last modified: November 03, 2003 [cit. 2008-09-02]. Accessible on WWW: <`http://www.uwlax.edu/faculty/will/svd/index.html`>. [cited at page(s) 29]

Appendices

Appendix A

Microstructure Micrographs, FEM Modelling Results

All included colour images in full resolution are accessible online at:
`http://files.glatz.cz/DP/app1/img`.

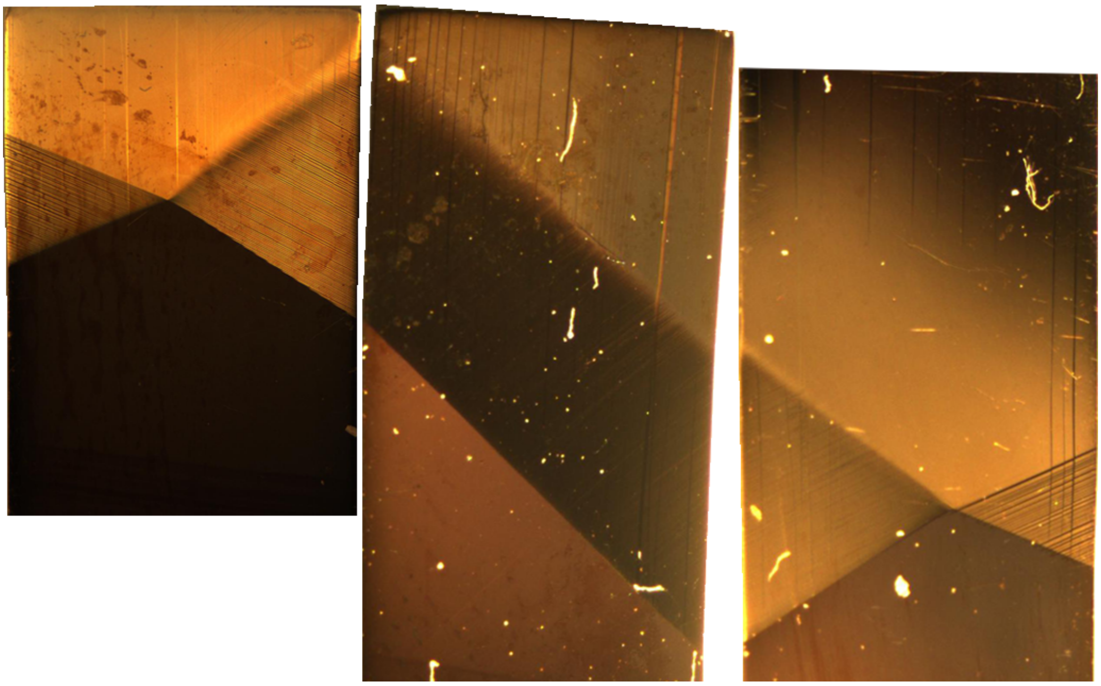

Figure A.1: Lambda microstructure (face A, B, and C)

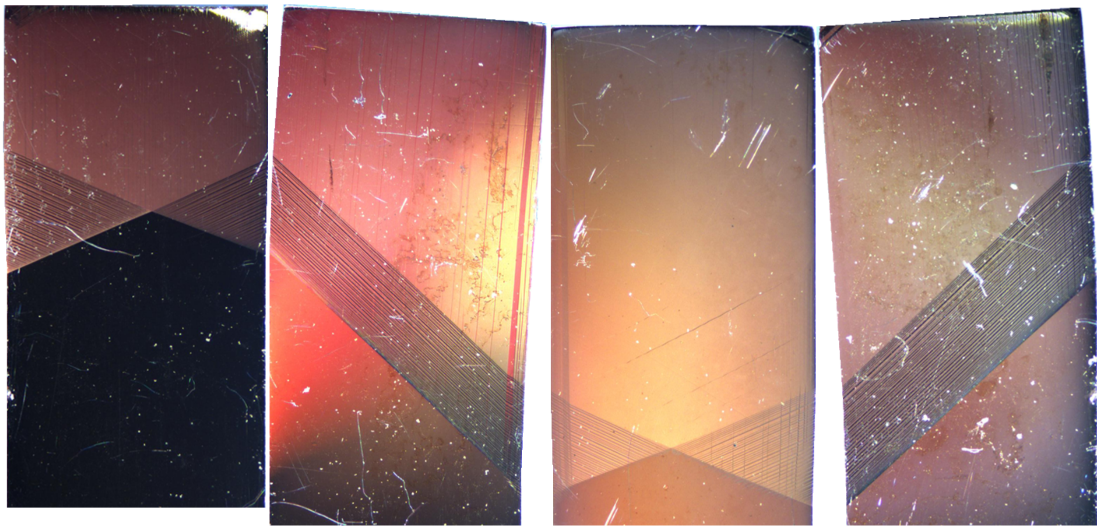

Figure A.2: Lambda microstructure (face A, B, C, and D)

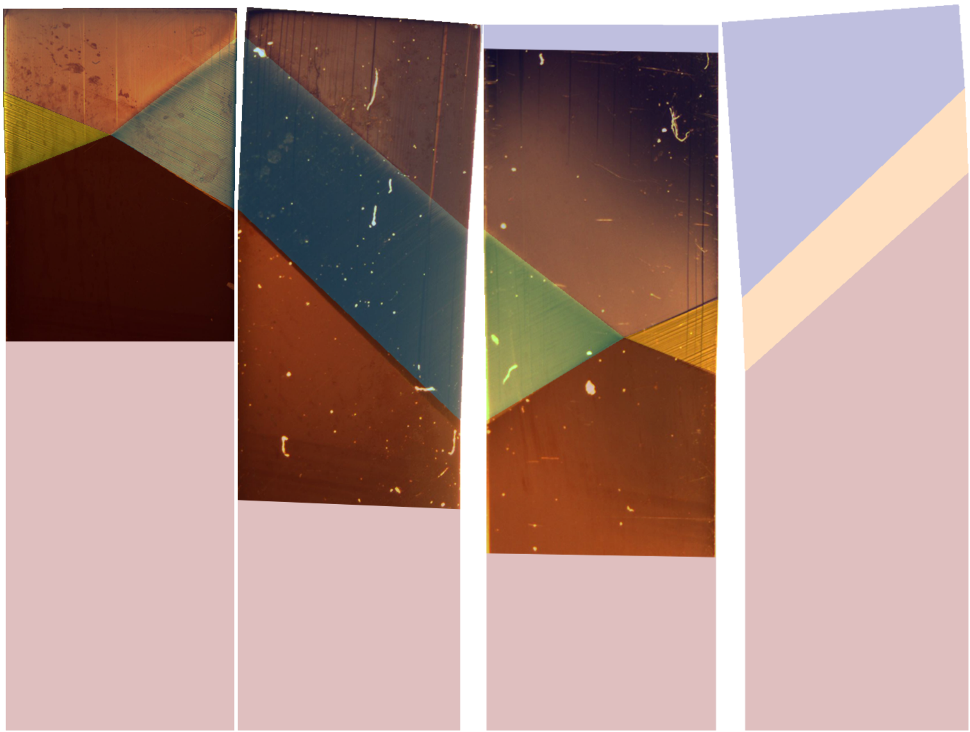

Figure A.3: Comparison of real and computed geometry of the lambda microstructure

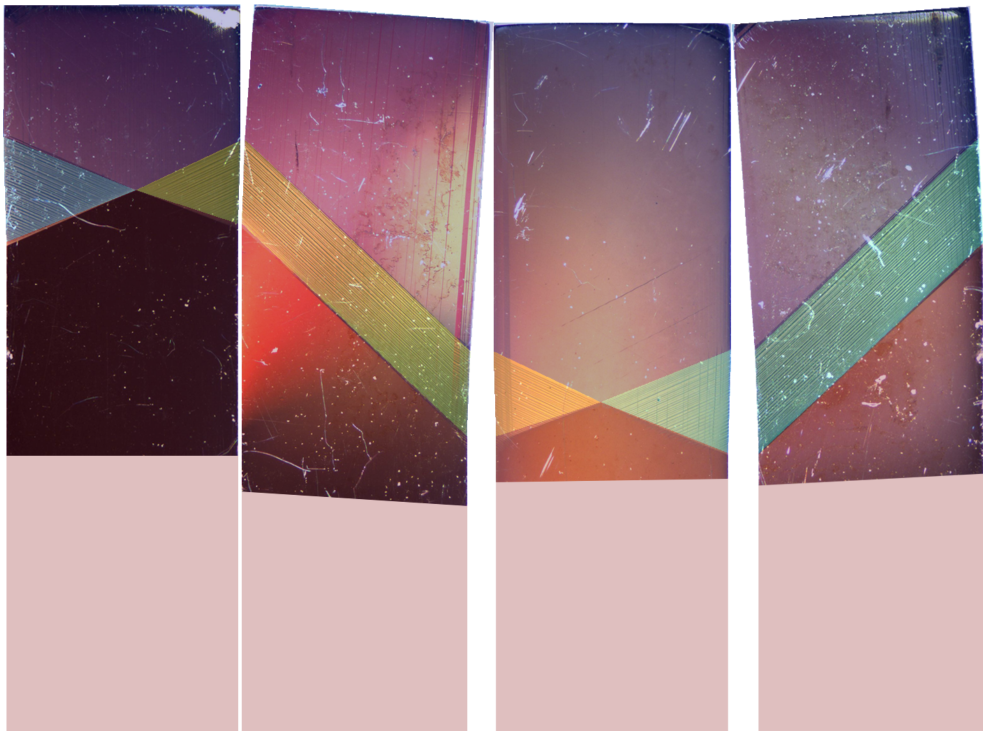

Figure A.4: Comparison of real and computed geometry of the X microstructure

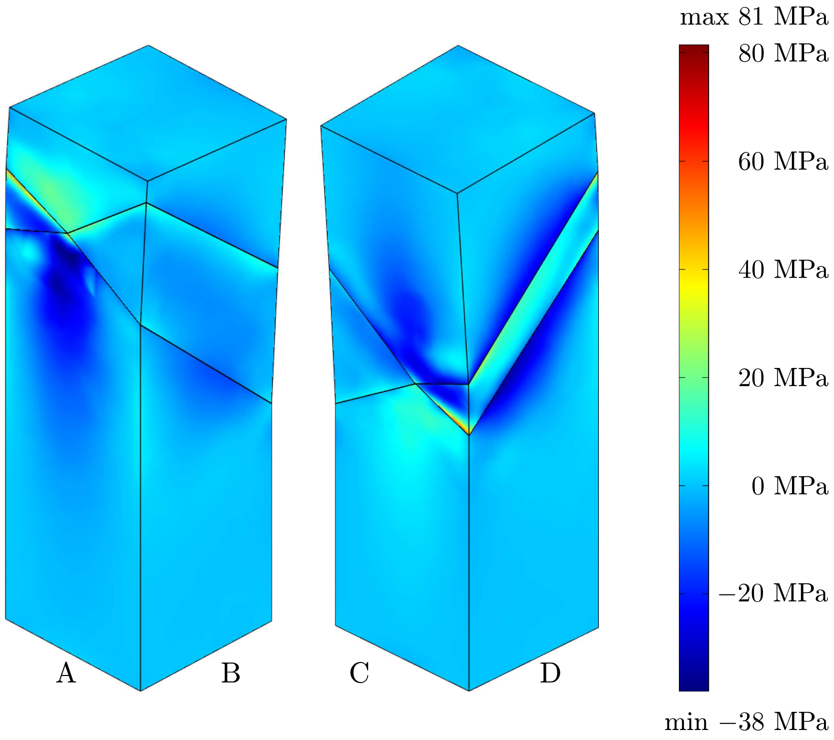

Figure A.5: Volume stress in the lambda microstructure

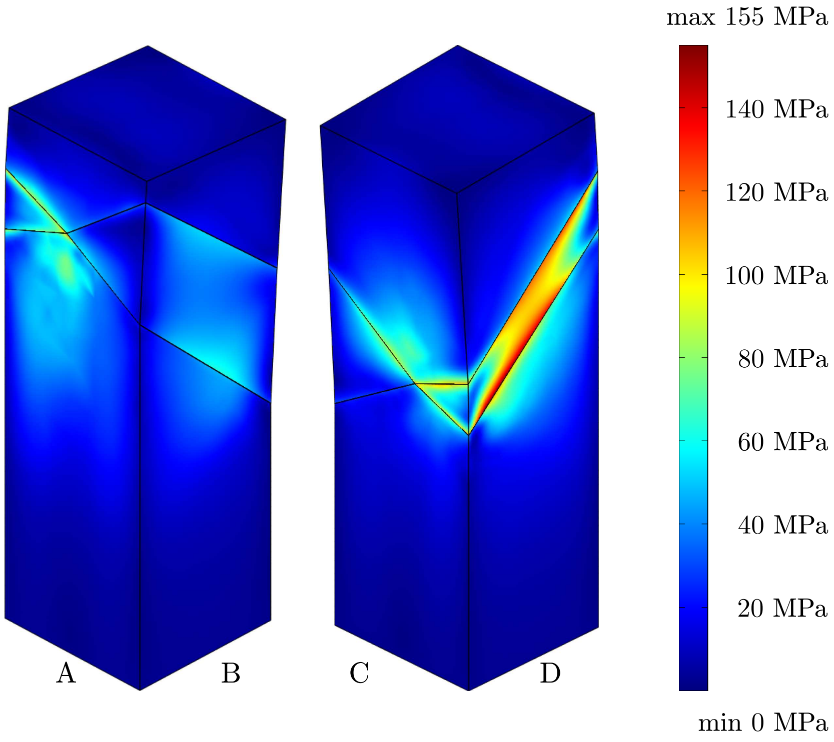

Figure A.6: Tresca stress in the lambda microstructure

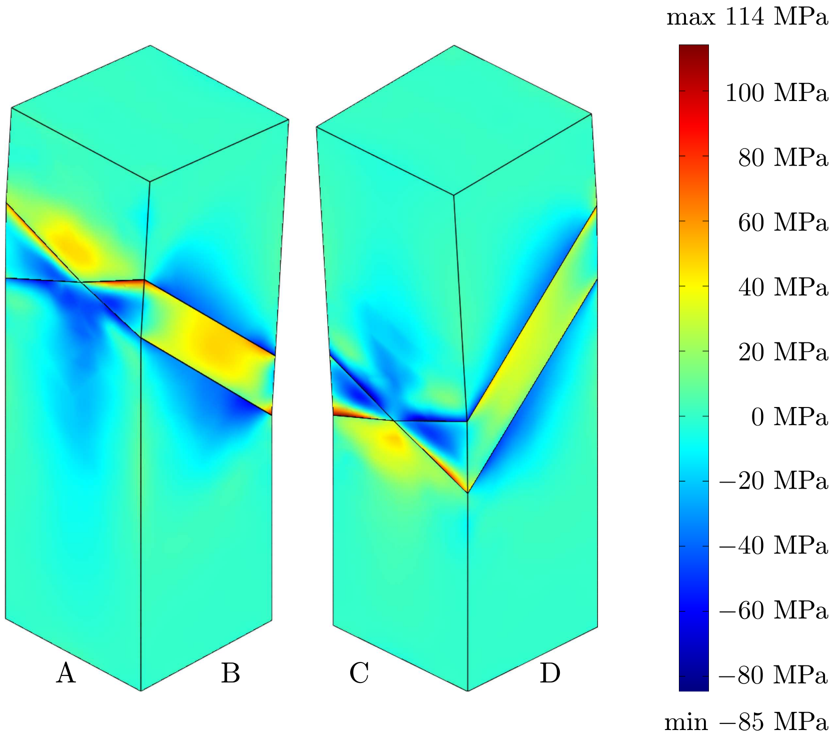

Figure A.7: Volume stress in the X microstructure

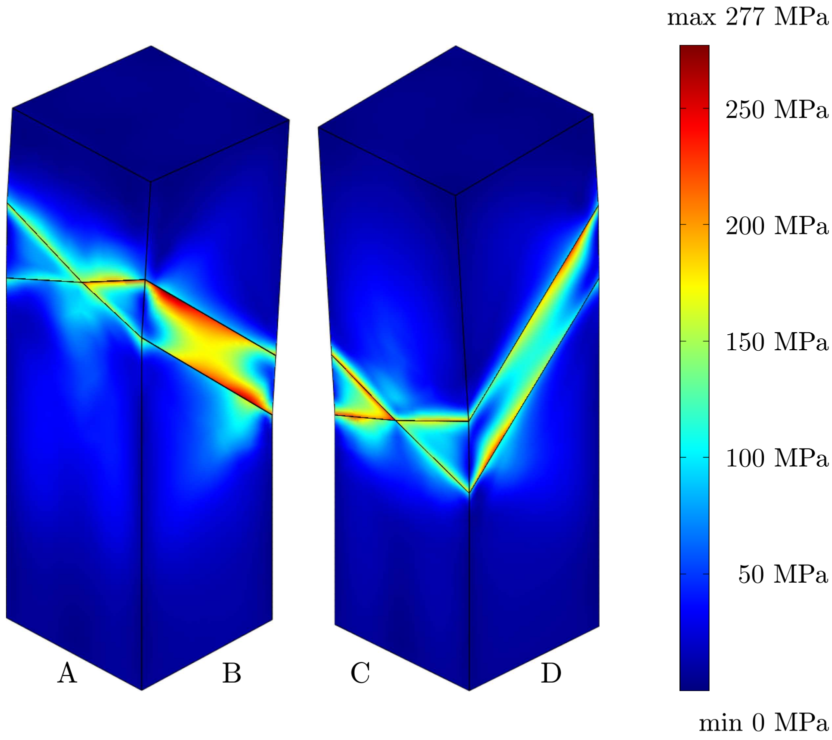

Figure A.8: Tresca stress in the X microstructure

List of Figures

List of Tables